The radial distribution of dust species in young brown dwarf discs

B. Riaz,[1]★ M. Honda,[2] H. Campins,[3] G. Micela,[4] M. G. Guarcello,[5] T. Gledhill,[1] J. Hough[1] and E. L. Martín[6]

[1]*Centre for Astrophysics Research, Science & Technology Research Institute, University of Hertfordshire, Hatfield AL10 9AB*
[2]*Department of Information Sciences, Kanagawa University, 2946 Tsuchiya, Hiratsuka, Kanagawa 259-1293, Japan*
[3]*Physics Department, University of Central Florida, Orlando, FL 32816, USA*
[4]*INAF – Osservatorio Astronomico di Palermo, Piazza del Parlamento 1, 90134 Palermo, Italy*
[5]*Smithsonian Astrophysical Observatory, MS-3, 60 Garden Street, Cambridge, MA 02138, USA*
[6]*Centro de Astrobiología (CSIC/INTA), 28850 Torrejón de Ardoz, Madrid, Spain*

ABSTRACT

We present a study of the radial distribution of dust species in young brown dwarf discs. Our work is based on a compositional analysis of the 10 and 20 μm silicate emission features for brown dwarfs in the Taurus–Auriga star-forming region. A fundamental finding of our work is that brown dwarfs exhibit stronger signs of dust processing in the cold component of the disc, compared to the higher mass T Tauri stars in Taurus. For nearly all of our targets, we find a flat disc structure, which is consistent with the stronger signs of dust processing observed in these discs. For the case of one brown dwarf, 2M04230607, we find the forsterite mass fraction to be a factor of ∼3 higher in the outer disc compared to the inner disc region. Simple large-scale radial mixing cannot account for this gradient in the dust chemical composition, and some local crystalline formation mechanism may be effective in this disc. The relatively high abundance of crystalline silicates in the outer cold regions of brown dwarf discs provides an interesting analogy to comets. In this context, we have discussed the applicability of the various mechanisms that have been proposed for comets on the formation and the outward transport of high-temperature material. We also present *Chandra* X-ray observations for two Taurus brown dwarfs, 2M04414825 and CFHT-BD-Tau 9. We find 2M04414825, which has an ∼12 per cent crystalline mass fraction, to be more than an order of magnitude brighter in X-ray than CFHT-BD-Tau 9, which has an ∼35 per cent crystalline mass fraction. Combining with previous X-ray data, we find the inner disc crystalline mass fractions to be anti-correlated with the X-ray strength.

Key words: stars: abundances – brown dwarfs – circumstellar matter – stars: low-mass.

1 INTRODUCTION

A study of the compositional alteration of dust grains in protoplanetary discs allows us to understand the conditions that initiate the formation of planets. The most dominant dust species in the circumstellar material are oxygen-rich silicates, which are either olivines ($Mg_{2x}Fe_{2(1-x)}SiO_4$), ranging from fayalite ($x = 0$) to forsterite ($x = 1$), or pyroxenes ($Mg_xFe_{(1-x)}SiO_3$), ranging from ferrosillite ($x = 0$) to enstatite ($x = 1$) (e.g. Kessler-Silacci et al. 2005). The spectra of silicate dust have vibrational spectral features near 10 μm (covering ∼8–14 μm wavelengths), due to the Si–O stretching mode, and near 20μm (covering ∼15–35μm wavelengths), due to the O–Si–O bending mode. Several previous studies on silicate dust composition in circumstellar discs have been based on the 10μm Si–O feature,

which probes the warm inner regions in a range of a few 100 to ∼1000 K and radii of within a few au in a typical T Tauri disc. In comparison, the 20μm spectral feature probes cold dust in the outer zone of the disc, where temperatures are expected to be less than a few hundred kelvin. Both features probe the optically thin surface layers of the disc. This difference in the location of the silicate emission zone can be utilized to study any radial dependence of the dust chemical composition, as well as processes such as turbulent diffusion and large-scale circulation that would result in the mixing of disc material from the warm inner to the cold outer regions, thereby reducing any radial concentration gradients.

Silicate dust in the interstellar medium (ISM) is observed to be almost entirely amorphous in composition, with negligible crystalline fractions (<1–2 per cent; Kemper, Vriend & Tielens 2004; Li, Zhao & Li 2007). Amorphous dust can be thermally annealed into crystalline dust at temperatures above ∼800 K (e.g. Fabian et al. 2000). However, crystalline silicates have been found in high

abundances in comets and meteorites, which are formed in regions much colder than 800 K. This suggests that some radial mixing took place between the inner and outer parts of the solar nebula during the early formation phase of our Solar system (e.g. Nuth, Hill & Kletetschka 2000; Wooden 2008). The presence of crystalline grains in cold regions could also be due to in situ heating events, such as the disc shocks proposed by Harker & Desch (2002). Recent compositional studies based on both the 10 and 20 μm silicate features for large samples of solar mass T Tauri stars have indicated nearly equal, and in a few cases, even higher crystalline grain abundances in the cold component of the disc compared to the inner warm regions (e.g. Kessler-Silacci et al. 2006; Sargent et al. 2009a; Watson et al. 2009). This has been explained by thermal annealing in the warm part followed by efficient radial transport to the cold outer disc. The analysis of *Stardust* samples from comet Wild 2 also support the view of processing of silicates near the Sun and then extensive mixing with much lower temperature materials such as cometary ices (e.g. Brownlee et al. 2006; Zolensky et al. 2006). Large-scale radial mixing, however, cannot explain radial gradients in dust chemical composition as observed for a few cases among solar-type stars and Herbig Ae/Be stars (e.g. van Boekel et al. 2004; Bouwman et al. 2008). A radial dependence in the relative abundances of the crystalline dust species instead suggests a localized crystalline formation mechanism. A local temporal heating process such as shock heating or grain–grain collision could raise the temperature sufficiently to cause crystallization, followed by slow cooling in an optically thick and turbulent disc environment (e.g. Molster et al. 1999). However, Harker & Desch (2002) have addressed the cooling issue for heated grains in shocks in (ordinarily) cool disc regions. They conclude that making the region optically thick does not slow down the cooling enough. Desch & Connolly (2002) conclude that it is the hot gas that keeps the grains warm, while the gas cools slowly, at rates comparable to the slow rates of cooling inferred for chondrules. Alternately, the crystallization process could occur in low-temperature environments induced by exothermic chemical reactions (e.g. Tanaka, Yamamoto & Kimura 2010). Such external processes could affect the time-scales over which dust processing proceeds in the different regions of the disc.

In the substellar mass domain, Riaz (2009; hereafter R09) presented compositional fits to the 10 μm silicate emission features for 23 brown dwarf discs in the Taurus–Auriga (∼1 Myr; Kenyon & Hartmann 1995) and Upper Scorpius (∼5 Myr; Preibisch & Zinnecker 1999) star-forming regions. Collectively, this sample provided an opportunity to probe any age dependence of the different dust processing mechanisms. We had found the detection rate for emission in the 10 μm silicate feature to decline with age, with only 20 per cent of the brown dwarfs at ∼5 Myr showing any detectable emission in the feature. The median crystalline mass fraction for the Taurus brown dwarfs was found to be a factor of ∼2 higher than the median reported for the higher mass stars in Taurus, indicating crystallinity to be more prominent in the warm inner regions of circum(sub)stellar discs. For most objects, we had obtained nearly equal mass fractions for the large and crystalline grains, and only 5 per cent of the Taurus brown dwarfs were found to be dominated by pristine ISM-like dust. This indicated that both the grain growth and crystallization processes are active in these discs, and significant dust processing has already occurred for most systems by a young age of ∼1 Myr. The R09 work was focused on the 10 μm feature only, and we could not study any radial dependence of the dust chemical composition. Among brown dwarf discs, there have been mainly two studies that have focused on the 20 μm silicate

emission feature. Merín et al. (2007) and Bouy et al. (2008) presented compositional studies of two young brown dwarf discs in the Lupus and Taurus star-forming regions, respectively, and found weak evidence of a decline in grain growth or the crystallinity levels when comparing the mass fractions in the inner and the outer parts of the disc. In the present study, we have analysed 20 μm silicate spectra for 13 brown dwarf discs in Taurus, which is the largest sample studied so far to probe the cold dust composition. This provides us with an opportunity to study the radial distribution of dust species for a large sample of brown dwarf discs, and to investigate if the crystalline formation and radial transport mechanisms are as efficient in the substellar domain as observed among the T Tauri systems.

2 OBSERVATIONS AND DATA REDUCTION

2.1 *Spitzer* IRS Observations

We searched the *Spitzer* IRS archives for 20 μm silicate spectra for the 20 Taurus brown dwarf discs studied in R09. These sources are spectroscopically confirmed members of Taurus with spectral types (SpT) of ≥M6, making these more likely to be substellar objects (e.g. Luhman 2004), and are known to show excess emission in the *Spitzer*/IRAC and MIPS bands, thus confirming the presence of discs around them (Luhman et al. 2010). We were able to find 20 μm spectra for 18 out of the 20 sources. The *Spitzer* PIDs for these observations are 30 540, 2, 248 and 20 435. Five of these show 'flat' features at both 10 and 20 μm, i.e. there is no detectable emission in the silicate features and only the underlying continuum is detected. We have not considered these flat spectra in our study. Our work is thus based on 20 μm spectra for a sample of 13 brown dwarf discs. The spectra were obtained in the IRS low spectral resolution modules, short–low (SL) and long–low (LL) ($\lambda/\delta\lambda \sim 90$). The SL module covers 5.2–14.5 μm in two orders, and the LL module covers 14–38 μm, also in two orders. The observations were obtained at two nod positions along each slit. The basic calibrated data were produced at the Spitzer Science Center (SSC) by the S15.3 pipeline for the SL module and the S17.2 pipeline for the LL module. The sky background was removed from each spectrum by subtracting observations taken in the same module, but with the target in the other order. The spectra were extracted and calibrated using the Spitzer IRS Custom Extraction (SPICE) software provided by the SSC. The extraction was performed using a variable-width column extraction that scales with the width of the wavelength-dependent point spread function (PSF). We used the SPICE 'optimal' extraction algorithm that yields a minimal-noise, unbiased flux estimate in each wavelength bin by weighting the extraction by the object profile and the signal to noise of each pixel. The optimal extraction provides greater improvement over regular extraction for low signal-to-noise ratio (S/N) data. Gains in S/N up to a factor of 2 have been achieved for sources with S/N ∼ 3, corresponding to an effective quadrupling of the exposure time. The rectified flux and uncertainty products written out by the optimal extraction algorithm include corrections for any offsets between different modules. Further details on the optimal extraction method are provided in the SPICE documentation. We have not applied any extinction correction since Taurus suffers from little reddening ($A_V < 1$ mag; e.g. Luhman et al. 2010).

2.2 *Chandra* X-ray observations

The brown dwarfs 2M04414825 and CFHT-BD-Tau 9 have been observed with *Chandra*/ACIS-S in the *very faint* mode, using the

Table 1. X-ray properties of 2M04414825 and CFHT-BD-Tau 9.

Source	RA (J2000)	Dec (J2000)	Θ^a (arcmin)	Net counts	$\sigma_{net\ counts}$	bkg counts[b]	PB[c]	E_{25}[d]	E_{50}[d]	E_{75}[d]	nH (10^{22} cm^{-2})	kT (keV)	$\log(L_X)$
2M04414825	70.451042	25.575151	0.3	373	20	18	0	1.03	1.26	1.76	0.36	1.5	29.315
CFHT-BD-TAU 9	66.110222	26.830584	0.3	7	2	6	4×10^{-8}	0.82	0.88	1.34	0.36	0.98	27.68

[a]Θ is the off-axis angle.

[b]bkg is for 'background'.

[c]*PB* is the probability associated with the hypothesis that the detected source is compatible with a background fluctuation.

[d]E_{25}, E_{50} and E_{75} are the 25 per cent, 50 per cent and 75 per cent quartiles of the photons median energy distribution.

back-illuminated CCD S3 (OBSID 12335 and 12336; P.I. Riaz). Data reduction has been made with CIAO 4.3 packages (Fruscione et al. 2006). The level 2 event files have been obtained from the level 1 event files retaining only events with grade = 0, 2, 3, 4, 6, *status* = 0, energy ranging from 0.3 to 8.0 keV, and removing the event position randomization introduced by the standard data processing, using the tasks `acis process events` and `dmcopy`. We calculated the exposure maps with the `merge all` task.

The source detection has been performed with PWDETECT (Damiani et al. 1997), using a threshold of $4.8\sigma_{sky}$, corresponding to one spurious source for each exposure. Both targets have an X-ray counterpart, with an offset equal to 0.22 (CFHT-BD-Tau 9) and 0.14 arcsec (2M04414825). CFHT-BD-Tau 9 is a weak source with a significance of 6, while 2M04414825 has a bright counterpart (significance > 50).

Photons extraction has been made using the IDL software ACIS EXTRACT[1] (AE; Broos et al. 2002), which uses TARA,[2] CIAO, FTOOLS[3] and MARX.[4] AE calculates the PSF for each source, and the source events are extracted in a region encompassing the 90 per cent of the PSF evaluated at 1.49 keV. Background events have been extracted for each source in circular annuli centred on the sources, which have been masked first covering the 99 per cent of the local PSF and then redefining a more accurate mask region.

The X-ray counterpart of 2M04414825 is bright enough to determine its parameters (the hydrogen column along the line of sight, nH, and the emitting plasma temperature, kT) fitting the observed spectra using XSPEC[5] v.12.6.0 (Arnaud, Borkowski & Harrington 1996). We assumed a plasma in a collisional ionization equilibrium thermal model with one temperature. The best-fitting model ($\chi^2_\nu = 0.93$) is a 1T thermal model with $kT = 1.5 \pm 0.2$ keV and $N_H = 0.36 \pm 0.09 \times 10^{22}$ cm^{-2}, corresponding to a visual extinction of $A_V = 2.01$, compatible with previous estimates of the extinction of Taurus members (e.g. Luhman et al. 2010). Using the 1T model and adopting a distance of 2M04414825 equal to 140 pc (Kenyon, Dobrzycka & Hartmann 1994), we obtained an X-ray luminosity equal to $\log(L_X) = 30.31$ erg s^{-1}.

The few counts detected from the X-ray counterpart of CFHT-BD-Tau 9 prevent us to perform a spectral fitting. In order to estimate the X-ray luminosity of this source, we set nH to the value derived from the typical extinction of Taurus members ($A_V = 2 \pm 1$), corresponding to $N_H = 0.36 \pm 0.09 \times 10^{22}$ cm^{-2}. We adopt a coronal temperature of $kT = 1$ keV and find a conversion factor (PIMMS) of 3.9×10^{-12} erg cm^{-2}, which translates in $\log(L_X) = 28.30$ erg cm^{-2}. Note that the conversion factor may vary not more

than 20 per cent in the 2–20 MK range, while the statistical error ($\sim$40 per cent) dominates the final uncertainty in Lx. Table 1 lists the properties of the X-ray counterparts of the two brown dwarfs described in this section.

3 ANALYSIS

3.1 Modelling of silicate emission spectra

The 10 and 20µm features probe the surface layers at different radii in the disc. For a typical T Tauri disc, 95 per cent of the flux at 10µm comes from within $\sim$1au, while 95 per cent of the 20 µm flux comes from within $\sim$10au (Kessler-Silacci et al. 2006). Thus with a factor of $\sim$2 increase in the peak wavelength of the silicate feature (10–20 µm), there is a shift by a factor of $\sim$10 in the disc radii from which most of the emission arises. There is a difference in the location of the silicate emission zone for stars of different luminosities. For a brown dwarf disc, 95 per cent flux at 10µm arises from smaller radii of $\leq$0.1au, while 95 per cent flux at 20µm arises from radii within $\sim$1–2au (Kessler-Silacci et al. 2007; Bouy et al. 2008). For any system, both silicate features probe the surface layers of the disc. For a young brown dwarf disc, the location of the 20 µm silicate emission zone at relatively larger disc radii implies cooler surface temperatures of <100 K, while smaller radii of $\leq$0.1au probed by the 10µm feature imply warmer surface temperatures of 300 K or higher (e.g. Merín et al. 2007). At the inner edge of the disc close to the central substellar source, dust sublimation temperatures of $\sim$1500 K can be reached (e.g. Whitney et al. 2003). Due to this, the silicate emission zone probed by the 10µm feature is usually referred to as the 'warm' or 'inner' component of the disc, while the region probed by the 20 µm feature is referred to as the 'cold' or 'outer' component. The dust temperature, however, is not expected to be constant and could vary by more than $\sim$100 K over a certain silicate emission zone.

We used a similar method as described in R09 to model the 20µm silicate emission features for the targets. Five dust species were considered in order to obtain a compositional fit to the observed spectra: amorphous olivine and pyroxene, crystalline enstatite, crystalline forsterite and silica. The characteristics of these are outlined in Table 2, and the spectral profiles plotted in Fig. 1. The bulk densities listed in Table 2 have been obtained from Bouwman et al. (2001). The amorphous grains show little dependence on shape (e.g. Bouwman et al. 2001) and thus can be assumed to be homogeneous and spherical so that the standard Mie theory can be applied to determine their spectroscopic properties. The properties of crystalline silicates however are sensitive to the grain shape which makes it important to consider shapes other than homogeneous spheres. Min, Hovenier & de Koter (2003) have studied the absorption and scattering properties of particles that are inhomogeneous in structure and composition,

[1] http://www2.astro.psu.edu/xray/docs/TARA/ae_users_guide.html

[2] http://www.astro.psu.edu/xray/docs/TARA

[3] http://heasarc.gsfc.nasa.gov/docs/software/ftools

[4] http://space.mit.edu/CXC/MARX/

[5] http://heasarc.nasa.gov/xanadu/xspec/

Table 2. Characteristics of the grain species used for the fitting procedure.

Species	Composition	Size (μm)	Shape	Reference	ρ_b (g cm^{-3})
Amorphous olivine	$MgFeSiO_4$	0.1 & 2.0	Homogeneous spheres	Dorschner et al. (1995)	3.71
Amorphous pyroxene	$Mg_{0.8}Fe_{0.2}SiO_3$	0.1 & 2.0	Homogeneous spheres	Dorschner et al. (1995)	3.71
Crystalline forsterite	$Mg_{1.9}Fe_{0.1}SiO_4$	0.1	Irregular (CDE)	Fabian et al. (2001)	3.33
Crystalline enstatite	$MgSiO_3$	0.1	Irregular (CDE)	Jäger et al. (1998)	2.80
Amorphous silica	SiO_2	0.1	Irregular (CDE)	Fabian et al. (2000)	2.21
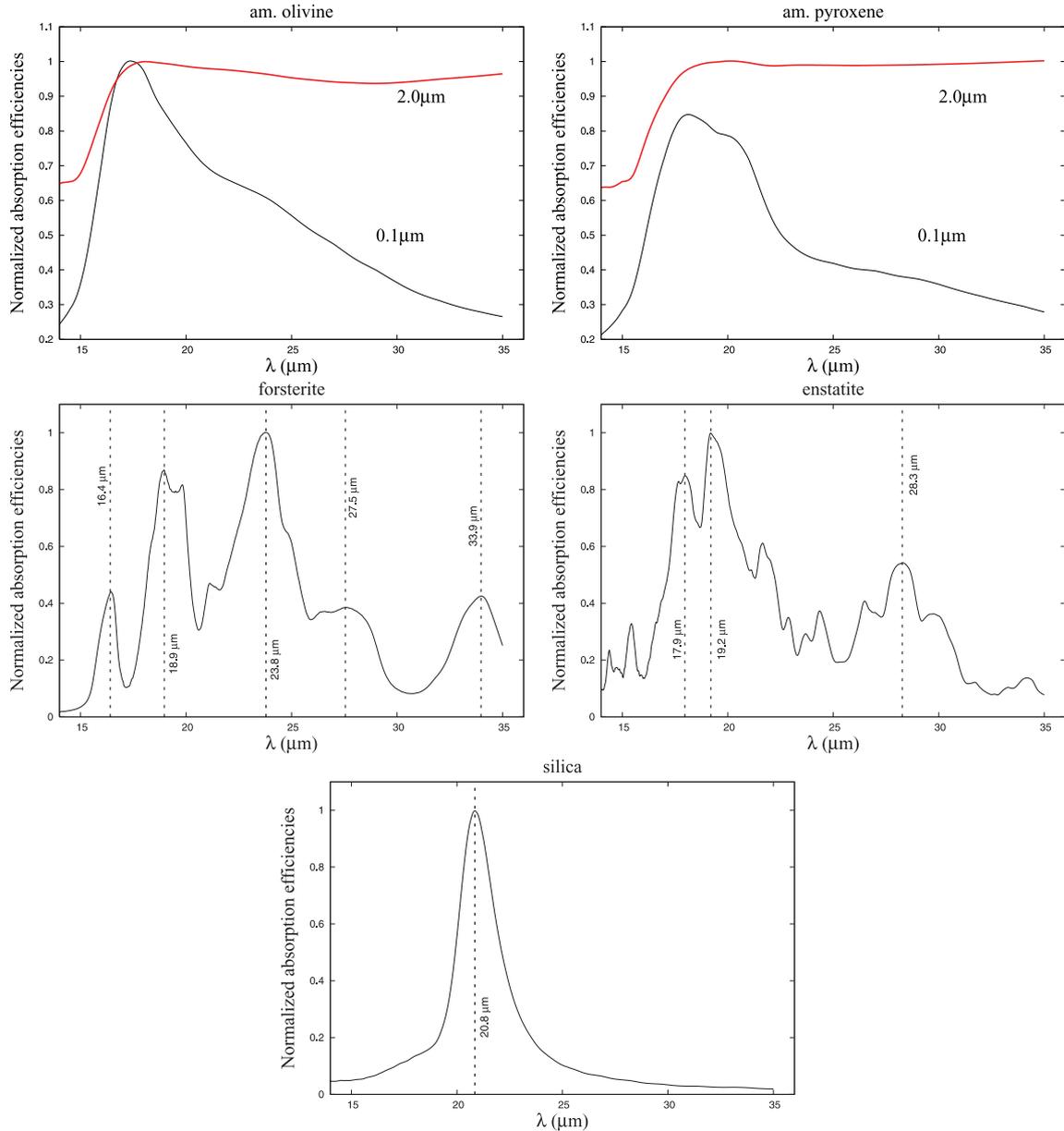
Figure 1. Normalized spectral profiles for the five dust species considered for modelling. The upper panel shows the profiles for small and large amorphous olivine and pyroxene silicates for grain sizes of 0.1 μm (black) and 2.0 μm (red). The middle and bottom panels show the profiles for forsterite, enstatite and silica grains. Prominent emissivity peaks are marked by dashed lines.

based on the assumption that the characteristics of such irregularly shaped particles can be simulated by the average properties for a distribution of shapes, such as ellipsoids, spheroids or hollow spheres. We considered both the distribution of hollow spheres (DHS) and the continuous distribution of ellipsoids (CDE) from

Min, Hovenier & de Koter (2003) and found a better match both in terms of the location and width of the spectral profiles using the CDE routine. Therefore the absorption efficiencies of crystalline silicates (enstatite and forsterite) and silica have been calculated using ellipsoidal grains. Since the CDE method has been used, the

grains are treated in the 'Rayleigh limit', i.e. the grain sizes are assumed to be much smaller than the wavelength of radiation. Our model is therefore biased towards submicron (0.1 μm) sized crystalline grains, and the effects of grain growth could not be studied for these species. For the case of amorphous silicates, two grain sizes of 0.1 and 2.0 μm have been used. As discussed in Bouwman et al. (2001), the optical properties of dust grains with a range in sizes between 0.01 and 5 μm can be characterized by two typical grain sizes: 0.1 μm for 'small' grains with sizes <1 μm and 2.0 μm for 'large' grains with sizes >1 μm.

To construct a model spectrum, we have followed the method outlined in R09 and Honda et al. (2003), wherein a power-law source function is assumed and the model flux F_λ is the sum of the emission from a featureless power-law continuum and the emission from the different dust species. We have considered a power-law continuum since it represents a sum of blackbody emission at various temperatures. It is unlikely for the dust temperature to remain constant over an ~20 μm wide spectral range. A power-law continuum provides a better approximation than using a single blackbody function at a fixed temperature to fit the continuum. The model spectrum can be written as

$$\lambda F_\lambda = a_0 \left(\frac{\lambda}{20\,\mu m}\right)^n + (a_1 Q_{0.1ao} + a_2 Q_{2.0ao}$$
$$+ a_3 Q_{0.1ap} + a_4 Q_{2.0ap} + a_5 Q_{ens} + a_6 Q_{fors}$$
$$+ a_7 Q_{sil}) \left(\frac{\lambda}{20\,\mu m}\right)^m , \qquad (1)$$

where $Q_{0.1ao}$ and $Q_{2.0ao}$ are the absorption efficiencies for 0.1 and 2.0 μm amorphous olivine, $Q_{0.1ap}$ and $Q_{2.0ap}$ are the absorption efficiencies for 0.1 and 2.0 μm amorphous pyroxene and Q_{ens}, Q_{fors} and Q_{sil} are the absorption efficiencies for enstatite, forsterite and silica, respectively. The free parameters in the model are the multiplicative factors a_1–a_7 in 10^{-14} W m^{-2} and two spectral indices of the source function, m and n. To correctly define the continuum level, we fixed the parameter a_0 to the observed flux density at 14–15.5 μm. We selected this wavelength range to be the continuum-fiting region as it is least affected by features in the spectra. To fit the model spectrum, we used the χ^2 minimization method outlined in van Boekel et al. (2005). The best-fitting values thus obtained for the multiplicative factors were used to derive the mass fractions. Table 3 lists the mass fractions for the amorphous and crystalline silicates. The 10 μm mass fractions are from R09. The uncertainties for the fit parameters were obtained by considering the errors on the observed fluxes, as well as the S/N. The errors on the observed fluxes are between ~1 and 8 per cent of the observed flux density, but are higher (15–20 per cent) in the ~30–35 μm wavelength range. We used the Monte Carlo method for error estimation as outlined in van Boekel et al. (2005) and discussed further in Juhász et al. (2009). In this method, random Gaussian noise is added to the spectrum, with 1000 synthetic spectra generated and fitted at each noise level. We considered four different noise levels with an $F_\nu^{error}/F_\nu^{observed}$ of 0.2, 0.1, 0.01 and 0.001, corresponding to an S/N of 5, 10, 100 and 1000, respectively. The mean of the resulting distribution of all fit parameters then corresponds to the best-fitting value, and the errors are derived from the standard deviation.

In order to validate our method, we modelled some known low-mass young objects and compared our results with those published in the literature. Our mass fractions are consistent with the fractions reported by Sargent et al. (2009a) for T Tauri discs in Taurus. These authors have also considered submicron sized crystalline grains in their model and have used the CDE distribution for grain

Table 3. Dust properties in the inner and outer disc.

Name	SpT[a]	Inner disc (10 μm) Small[c] (per cent)	Inner disc (10 μm) Large[d] (per cent)	Inner disc (10 μm) Crystalline [ens; fors][e] (per cent)	Outer disc (20 μm) Small (per cent)	Outer disc (20 μm) Large (per cent)	Outer disc (20 μm) Crystalline [ens; fors] (per cent)	R_{in} [R_{sub}][b]	Inclination[b]	β[b]
2MASS J04141188+2811535	M6.25	33.2 ± 10	39.5 ± 5	22.7 ± 7 [8.2 ± 4; 14.5 ± 6]	27.2 ± 8	40.5 ± 14	28.5 ± 8 [9.7 ± 5; 18.8 ± 6]	8.8	70–80°	1.172
2MASS J04141760+2806096	M5.5	81.4 ± 7	10.5 ± 6	4.7 ± 3 [0.0001 ± 0.5; 4.7 ± 3]	58 ± 8	18.4 ± 11	20.1 ± 8 [7.4 ± 4; 12.7 ± 7]	2.95	50–60°	1.144
V410 X-ray 6	M6	85.6 ± 8	14.3 ± 5	0.009 ± 0.6 [0.004 ± 0.6; 0.005 ± 0.6]	60.6 ± 9	19.7 ± 7	14.3 ± 5 [9.2 ± 4; 5.1 ± 3]	118.5	70–80°	1.06
2MASS J04230607+2801194	M6.5	56.2 ± 8	4.2 ± 5	38.5 ± 8 [24.7 ± 7; 13.8 ± 4]	0.0004 ± 11	21.9 ± 18	56.9 ± 15 [11.6 ± 8; 45.4 ± 13]	1.0	50–60°	1.16
CFHT-BD-Tau 20	M5.5	41.7 ± 10	0.013 ± 9	49.9 ± 13 [25.2 ± 9; 24.7 ± 10]	1.6 ± 9	46.2 ± 16	37.2 ± 12 [14.8 ± 10; 22.4 ± 7]	1.0	50–60°	1.103
CFHT-BD-Tau 9	M6.25	44.6 ± 5	18.2 ± 6	29.6 ± 4 [17.2 ± 2; 12.4 ± 4]	0.0001 ± 14	59.8 ± 14	26.1 ± 8 [13.5 ± 8; 12.6 ± 8]	1.0	30–40°	1.1
2MASS J04400067+2358211	M6.5	59.7 ± 6	5 ± 3	24.8 ± 6 [15.3 ± 4; 9.4 ± 5]	0.0006 ± 10	63.4 ± 12	28.7 ± 7 [10.1 ± 4; 18.5 ± 6]	1.0	50–60°	1.185
GM Tau	M6.5	51.1 ± 8	30.2 ± 4	15.7 ± 5 [0.001 ± 2; 15.7 ± 5]	2.6 ± 11	47.7 ± 19	43.3 ± 10 [17.1 ± 10; 26.2 ± 10]	1.0	70–80°	1.03
2MASS J04554801+3028050	M5.6	39.2 ± 5	31.2 ± 7	16.7 ± 10 [16.7 ± 10; 0.0005 ± 2]	0.0002 ± 11	52.4 ± 18	19.9 ± 14 [17.3 ± 12; 2.6 ± 7]	1.0	30–40°	1.1
MHO 5	M6.2	13.5 ± 4	63.7 ± 11	22.5 ± 5 [10.5 ± 3; 12 ± 4]	–	–	–	1.0	30–40°	1.13
CFHT-BD-Tau 8	M6.5	72.2 ± 7	0.004 ± 5	20.4 ± 6 [8.2 ± 4; 12.2 ± 5]	–	–	–	1.0	70–80°	1.12
2MASS J04290068+2755033	M8.25	41.3 ± 3	18.6 ± 7	36.3 ± 7 [17.6 ± 4; 18.7 ± 6]	–	–	–	17.9	70–80°	1.06
2MASS J04242090+2630511	M7	66.5 ± 11	24.4 ± 15	1.1 ± 2 [0.55 ± 2; 0.55 ± 2]	–	–	–	1.0	30–40°	1.16

[a] References for SpT: Luhman 2004, 2006, Luhman et al. 2006, Martín, Delfosse & Guieu 2004. Uncertainty in SpT is ±0.25.
[b] Results for inner disc radius, R_{in}, the disc inclination, and the flaring power, β, form the best-fitting disc models. The unit for R_{in} is R_{sub}, the dust sublimation radius; 1R_{sub} ~ 0.0004 au.
[c] Percentage of small amorphous olivine and pyroxene silicates compared to all other silicates.
[d] Percentage of large amorphous olivine and pyroxene silicates compared to all other silicates.
[e] Percentage of submicron crystalline silicates (enstatite and forsterite) compared to all other silicates, including silica. The separate enstatite and forsterite fractions are listed in square brackets.

opacities, similar to the distribution used in our model. As discussed in R09 and Sargent et al. (2009a), large grains can be considered as heterogeneous aggregates, made up of submicron sized amorphous silicates, forsterite or enstatite, with the highest abundance of amorphous grains. The opacities of the forsterite components of such large heterogeneous grains have been shown by Min et al. (2008) to resemble the opacity of small homogeneous forsterite grains, whereas the opacity of the amorphous component of the aggregate is found to resemble that of large amorphous homogeneous grains, with a size comparable to that of the heterogeneous aggregate. Therefore modelling the crystalline component of a large heterogeneous aggregate with small crystalline grains should not result in largely erroneous mass fractions for the crystalline silicates. This is consistent e.g. with the findings of Bouwman et al. (2008), who have considered three different grain sizes of 0.1, 1.5 and 6.0 μm in their models, but have found the typical sizes from the model fits to be submicron for the crystalline silicates and 6 μm for the amorphous grains. We modelled some of the forsterite exemplars from the study of Sargent et al. (2009a), such as DK Tau and GN Tau. We find a crystalline mass fraction of 38 ± 10 per cent and 55 ± 12 per cent for DK Tau and GN Tau, respectively, with a small- and large-amorphous-grain mass fraction of 12 ± 8 per cent and 42 ± 13 per cent for DK Tau and 20 ± 10 per cent and 7 ± 5 per cent for GN Tau. For sources such as DM Tau or DO Tau that show negligible signs of grain growth in the disc, we find a small-grain mass fraction of $\sim$80–82 per cent and a crystalline fraction of 15 ± 9 per cent, with a large-grain fraction of <5 per cent. These fractions are consistent within the uncertainties with the values listed in Sargent et al. (2009a) for the cold component of the disc.

We also modelled the Taurus brown dwarf 2M04442713 discussed in Bouy et al. (2008) and obtained a large-grain and a crystalline mass fraction of 68 ± 8 per cent and 30 ± 11 per cent, respectively. These values are consistent with the mass fractions listed in Bouy et al. (2008) for the low-temperature polynomial continuum case. For the very low mass star SST-Lup3-1 discussed in Merín et al. (2007), we find a crystalline and large-grain mass fraction of 38 ± 13 per cent and 22 ± 10 per cent, respectively, which are comparable to the fractions reported by these authors for the high-continuum case. We note that a direct comparison of our results with those reported in Bouy et al. and Merín et al. is not appropriate, since these works have considered a different set of grain opacities (the DHS model), and therefore the input optical constants are different than the ones considered in our model.

3.2 Disc modelling

We have used the 2D radiative transfer code by Whitney et al. (2003) for disc modelling. The circumstellar geometry consists of a rotationally flattened infalling envelope, bipolar cavities and a flared accretion disc in hydrostatic equilibrium. The disc density is proportional to $\varpi^{-\alpha}$, where ϖ is the radial coordinate in the disc mid-plane, and α is the radial density exponent. The disc scale height increases with radius, $h = h_0 (\varpi / R_*)^\beta$, where h_0 is the scale height at R_* and β is the flaring power. For the stellar parameters, we used the T_{eff}–SpT relation from Luhman et al. (2003) to determine the stellar effective temperature. We have considered an age of $\sim$1 Myr for the Taurus–Auriga cluster (Kenyon & Hartmann 1995). The stellar mass and radius were obtained by considering the 1 Myr isochrone from Baraffe et al. (2003). The NextGen (Hauschildt, Allard & Baron 1999) atmosphere file for the appropriate T_{eff} and $\log g = 3.5$ was used to fit the atmosphere spectrum of the central substellar source. A distance of 140 pc (Kenyon et al. 1994) was used to scale the output fluxes from the models to the luminosity and distance of the brown dwarfs.

Fig. 2 (right-hand panel) shows the disc model fits obtained for the targets. Also indicated are the separate contributions from the disc and the stellar photosphere. The *Spitzer* IRAC and MIPS data points shown in the fit are from Luhman et al. (2010), the near-infrared (IR) points are the 2MASS data and the optical data have been obtained from SIMBAD. Detailed discussions on the fitting procedure and the variations in the model spectral energy distributions (SEDs) with the different disc parameters are provided in Riaz & Gizis (2007). Here we provide a brief description of the best model fits (based on the lowest reduced-χ^2 value) obtained for these brown dwarfs.

The disc models provide the capability to include different grains in different disc regions (see Whitney et al. 2003, fig. 1). There are three grain models supplied by the code: 'large' grains with a size distribution that decays exponentially for sizes larger than 50 μm up to 1 mm, the 'medium' sized grains of sizes with $a_{\text{max}} \sim 1$ μm and 'small' ISM-like grains with $a_{\text{max}} \sim 0.25$ μm. All three models consider a minimum grain size of 0.0025 μm. The large-grain model used by Whitney et al. (2003) is the same as used by Wood et al. (2002) to fit the HH 30 disc SED. The medium grain size distribution is the same grain model that Cotera et al. (2001) have used to model the HH 30 near-IR scattered light images. The ISM grain model is the same as used by Kim, Martin & Hendry (1994) from their mass distribution for the fit to the canonical ($R_v = 3.1$) average diffuse ISM. All three models are based on the method of a power law with exponential decay (PED) above some cut-off grain size a_c, as discussed in Kim et al. (1994; equation 3) and Wood et al. (2002; equation 4). For the large-grain model, the values for the exponents p and q of the PED are 3 and 0.6, respectively, and the cut-off and maximum grain sizes are $a_c = 50$ μm and $a_{\text{max}} = 1000$ μm. For the medium grain size model, $q = 1$, $p = 3.5$, $a_c = 0.55$ μm and $a_{\text{max}} = 20$ μm. For the diffuse ISM model, $a_c = 0.02$ μm and $a_{\text{max}} = 0.25$ μm, with the PED exponent $\gamma = -3.06$ for silicate grains (equation 3 of Kim et al. 1994).

We have varied these grain models in the disc mid-plane and the upper atmosphere in order to obtain a good fit to the silicate emission features and the overall SED. The model used here assigns large grains to the high-density regions. Due to this, when large grains are used in the disc mid-plane, similar grains are placed close to the inner wall since it is of high density. This affects the emission from the inner wall and hence the observed flux at 10 μm. Thus by using submicron sized grains in the disc mid-plane, we indirectly reduced the inner wall grain size, and were able to obtain a good fit to the 10 μm silicate feature. There could still be bigger grains in the really dense mid-plane region of the disc, the presence of which can be confirmed with far-IR/sub-mm observations. On the other hand, if this were a 'three-layered' disc model instead of a 'two-layered' one, large grains could be placed in the very dense regions without affecting the 10 μm feature. For most sources, good fits are obtained if submicron sized grains are placed in both the mid-plane and the disc surface layers. This produces a model SED with a more peaked emission at 10 μm and a steeper slope at far-IR/sub-mm wavelengths (e.g. Riaz & Gizis 2007). For MHO 5 that has a very flat disc structure, the large-grain model with a_{max} of 1 mm was considered in both the disc mid-plane and the atmosphere. This results in a flat silicate feature as well as a flat sub-mm slope in the model SED. Considering that we do not have any far-IR/sub-mm observations for these objects, the silicate features provide the only way to constrain the different grain sizes considered by these disc models.
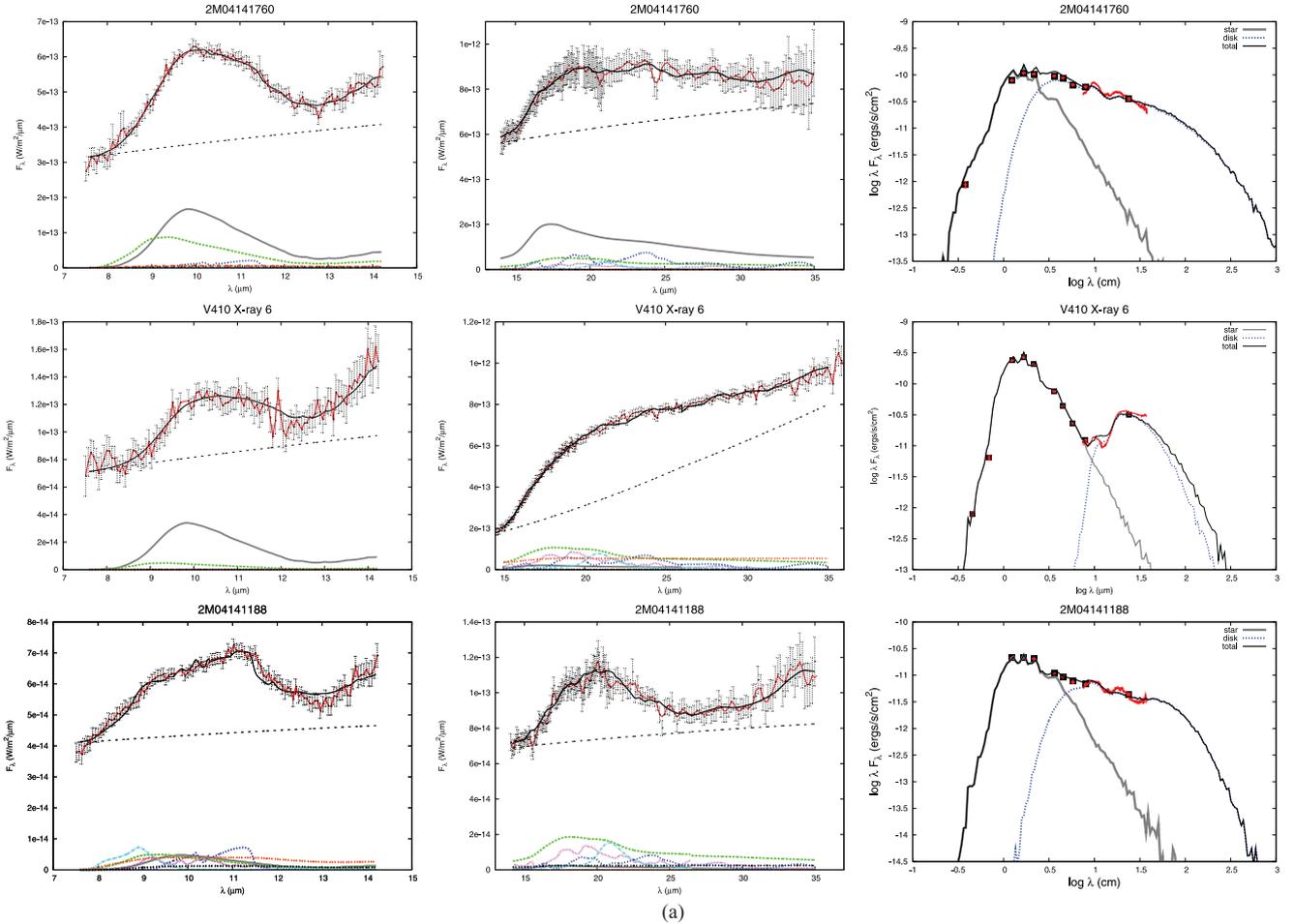
Figure 2. (a) Left and middle panels show the model fits to the 10 and 20μm silicate features, respectively. Colours represent the following: red – observed spectrum; black – model fit, grey – small amorphous olivine; green – small amorphous pyroxene; cyan – silica; blue – forsterite; pink – enstatite; black dashed – large amorphous olivine; orange – large amorphous pyroxene. The thin dashed line represents the continuum. The right-hand panel shows the model SED fit. The grey line represents the stellar photosphere contribution; disc emission is indicated by the blue line. (b) Model fits for discs with prominent forsterite features at 20μm. Symbol are the same as in Fig. 2(a). (c) Model fits for the four 'outliers' with negligible 20μm emission. The middle panel here shows the normalized continuum subtracted 20μm spectra in units of $(F_v - F_c)/F_c$. The dashed horizontal line represents the continuum. For the left and right panels, symbols are the same as in Fig. 2(a). (d) Model fits for the discs that show weaker features at 20μm. Symbol are the same as in Fig. 2(a).

There are degeneracies in the disc model fits presented here, considering that we have only ∼5–38μm data to model these discs. The uncertainties in the stellar parameters could also result in changes in the disc parameters. There are mainly six parameters related to the disc emission in these models, which can be varied to obtain a good fit. We had fixed the disc mass and the outer disc radius given the absence of longer wavelength data. The disc outer radius was fixed at 100au, and the disc mass for modelling was set to 1×10^{-4} M$_\odot$. This is the typical disc mass obtained by Scholz, Jayawardhana & Wood (2006) from 1.3 mm observations for a sample of Taurus brown dwarfs. We had fixed the disc mass accretion rate at 10^{-10} M$_\odot$ yr^{-1}, a typical value observed among accreting T Tauri stars (e.g. Muzerolle et al. 2003). It is, however, possible to constrain the amount of flaring in the disc, the inclination angle and the inner disc radius, using the available observations.

The disc scale height varies as $h = h_0(\varpi/R_*)^\beta$, where h_0 is the scale height at R_* and β is the flaring power. We varied both h_0 and β to determine the amount of flaring in these discs. The variations in the model SEDs as β is lowered are more evident for $\lambda > 10$μm, and the 24μm observation provides a good constraint to the flaring power. The model SED is highly flared for $\beta = 1.25$, which is

considered a typical value for models of T Tauri discs in hydrostatic equilibrium (e.g. Walker et al. 2004), while the structure is flat for $\beta = 1.0$ or smaller values (e.g. Riaz & Gizis 2007). For most sources, we were able to obtain good fits using $\beta \leq 1.1$ and $h_0 < 1$, indicating flat structures for these brown dwarf discs.

We have explored a range of inclination angles to the line of sight. Due to binning of photons in the models, there are a total of 10 viewing angles, with face-on covering 0–18° inclinations. The mid- and far-IR fluxes increase with decreasing inclinations, as the emission at these wavelengths is from an optically thick disc, while the optically thin millimetre fluxes are independent of the inclination (e.g. Riaz & Gizis 2007). We obtained good fits using intermediate inclinations of 50–60° for most discs (with a ±10° uncertainty). A few discs including V410 X-ray 6 are at a larger inclinations of >70° and can be considered as edge-on systems. Four discs including MHO 5 were fitted well using face-on inclinations of <40°, although MHO 5 has a very flat disc and the inclination would not really matter for such a flat system.

The inner disc radius, R_{in}, was varied as multiples of R_{sub}, where R_{sub} is the dust sublimation radius and varies with the stellar radius and temperature, $R_{sub} = R_*(T_{sub}/T_*)^{-2.085}$ (Whitney et al. 2003).
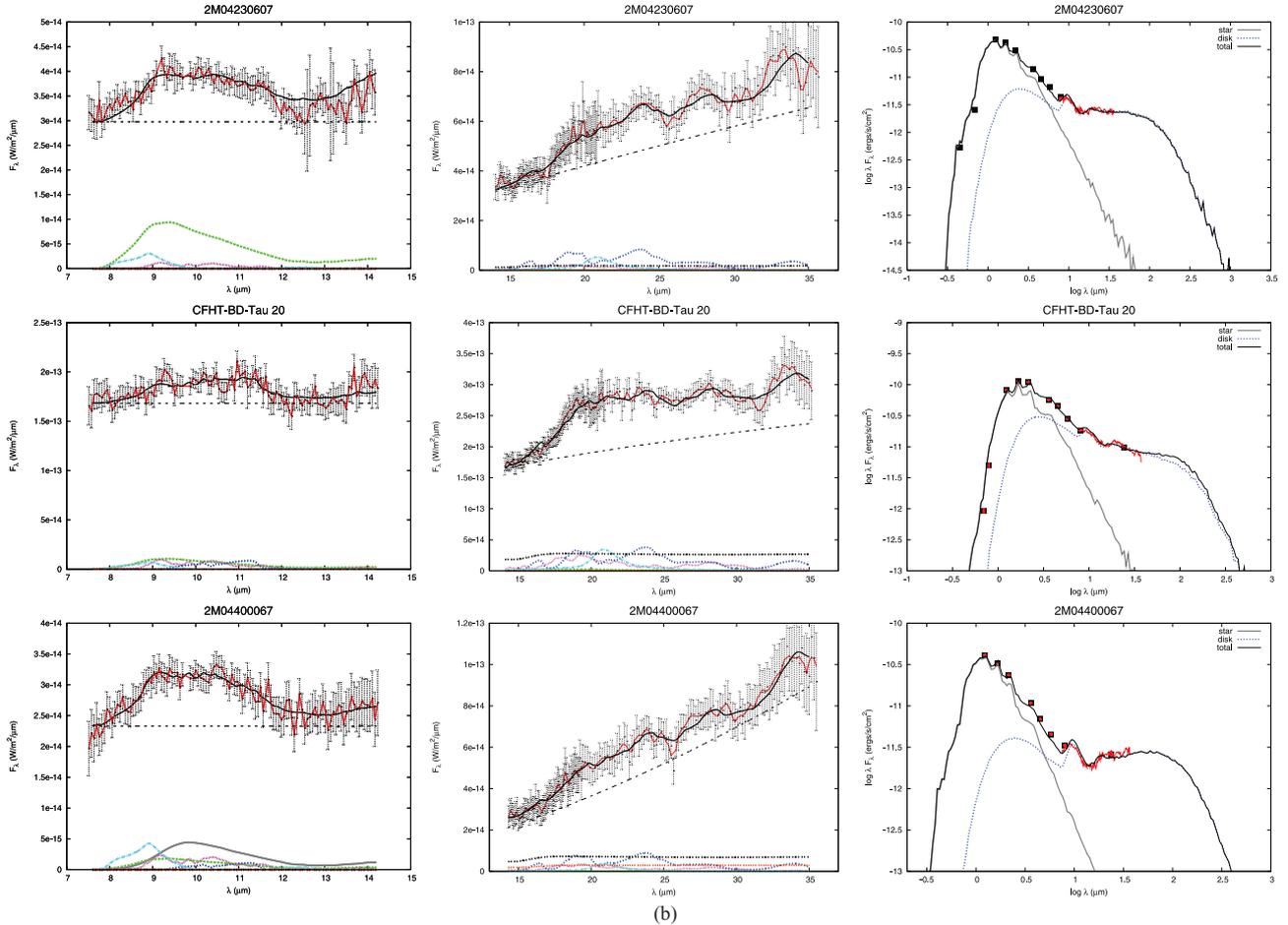
Figure 2 – *continued*

$T_{\rm sub}$ is the dust sublimation temperature and was set to 1600 K. Increasing the inner radius to 5 or $7R_{\rm sub}$ results in higher fluxes near the 10 μm silicate band and at longer wavelengths. For nearly all discs, we found a good fit using $R_{\rm in} = 1\ R_{\rm sub}$ ($\sim$0.0004 au). For the transition disc V410 X-ray 6, a larger inner disc radius of $\sim$0.05 au provided a good fit. The best-fitting values for these parameters are listed in Table 3.

4 RESULTS

4.1 The least processed discs: V410 X-ray 6 and 2M04141760

The brown dwarfs 2M04141760 and V410 X-ray 6 show a very smooth 20 μm feature, with a peak near $\sim$18 μm that is indicative of small amorphous olivine grains (Fig. 2a). The 10 μm spectra for both of these sources are also quite smooth with a peak at $\sim$9.8 μm indicative of small amorphous olivine grains, and no clear crystalline peaks are observed. We find a high small-grain mass fraction of >65 per cent in these discs, from both the 10 and 20 μm features, with a <5 per cent fraction of crystalline grains and <15 per cent fraction of large grains. The inner and outer regions of these discs thus show weak signs of dust processing.

The amount of crystalline silicates in a disc could be dependent on the presence of dense disc material in the inner disc regions. If crystalline silicates form due to thermal annealing of amorphous grains in the warm inner disc regions, and then are radially transported to the outer disc, then the presence of an inner hole in the disc could result in a reduction in the crystalline silicate production. This may be the case for V410 X-ray 6. This brown dwarf has a transition disc and displays photospheric emission up to wavelengths of $\sim$8 μm (Fig. 2a). From disc modelling, we estimate an inner disc hole of $\sim$118$R_{\rm sub}$ ($\sim$0.05 au). In comparison, 2M04141760 has a much smaller inner disc radius of $\sim$3$R_{\rm sub}$ ($\sim$0.001 au), but exhibits a similar lack of crystallinity in the disc. No clear correlation is thus seen between the presence of a large inner hole and low crystallinity in the disc.

The disc for V410 X-ray 6 flares up at wavelengths longward of $\sim$15 μm (Fig. 2a). Watson et al. (2009) find a trend in the Taurus T Tauri sample of more flattened discs having greater crystallinity. Also, Sargent et al. (2009a) find a possible weak trend in a similar sample of flattened discs tending to have higher large-grain mass fractions. The lack of crystallinity in V410 X-ray 6 is consistent with a flared geometry, indicating that the correlations noted by Watson et al. and Sargent et al. are also applicable to the substellar cases. As mentioned, the submicron amorphous grain fraction for V410 X-ray 6 and 2M04141760 is quite high (>60 per cent), and the large-grain mass fraction is only 15 per cent or less. These discs are at an early stage of evolution and significant dust processing has not yet occurred. This is more apparent from the SED for 2M04141760 that shows a strong excess emission even at 3.6 μm. Among the 65 T Tauri systems in Taurus studied by Sargent et al. (2009a) and Watson et al. (2009), 5 per cent are found to have high mass fractions of amorphous submicron grains >70 per cent, with weak signs of crystalline or large silicates. We have an $\sim$15 per cent
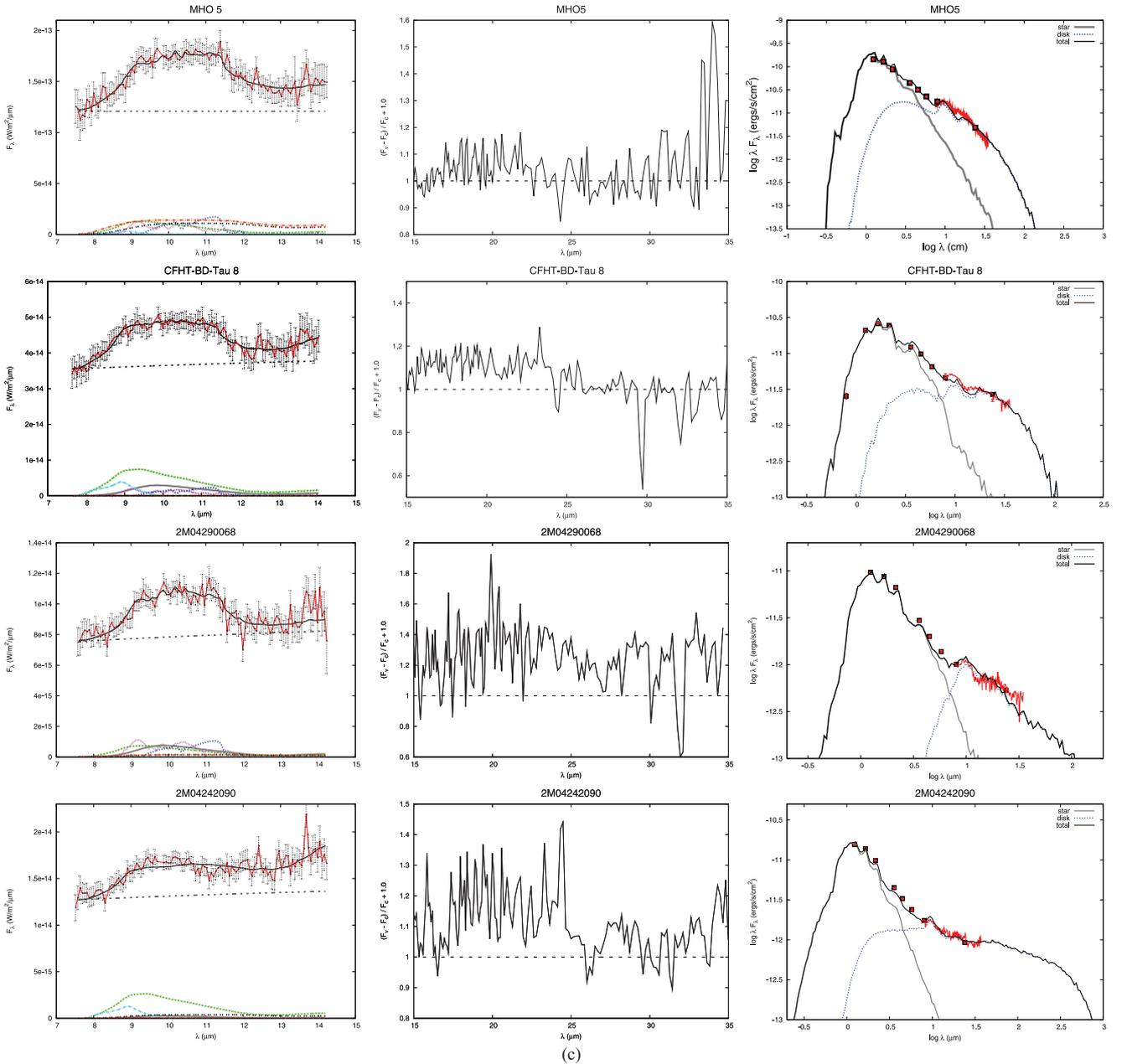
Figure 2 – *continued*

fraction of such systems in our Taurus brown dwarf sample that are still dominated by ISM-like grains.

The one property that is found to be different for these two sources is X-ray variability. Both V410 X-ray 6 and 2M04141760 show strong variations in X-ray emission, and have been classified as X-ray flaring sources (Grosso et al. 2007). In R09, we had noted a weak anti-correlation between the X-ray emission strength and the extent of crystallinity in the disc, suggesting that X-ray activity could affect the crystalline structure of the dust grains. We discuss this further in Section 5.3.

4.2 The mixed composition disc: 2M04141188

2M04141188 shows an interesting 20μm spectrum, with weak emission between ∼25 and 30μm. The spectrum shows a broad peak near ∼20μm and then a rise in emission longward of ∼30μm. There

may be a smaller peak near ∼33μm due to crystalline forsterite, although it may well be consistent with the point-to-point noise around that wavelength range. The broad feature near 20μm is well fitted using a model with a mixture of small amorphous and crystalline enstatite and forsterite grains, along with some contribution from amorphous silica. The 10μm spectrum for 2M04141188 shows a broad, trapezoidal shape with a crystalline forsterite peak near 11.3μm. Such shapes are indicative of grain growth and crystallization in the disc. We find roughly equal mass fractions of ∼30–50 per cent for the small and large amorphous, and the crystalline silicate grains. The fractions are similar in the inner and outer disc regions. This disc thus exhibits a mixed composition in both the warm and cold disc regions.

The 'dip' observed in the 20μm spectrum between ∼25 and 30μm could be due to obstruction by the bright edge of the disc. The best-fitting disc model for 2M04141188 indicates a close to edge-on
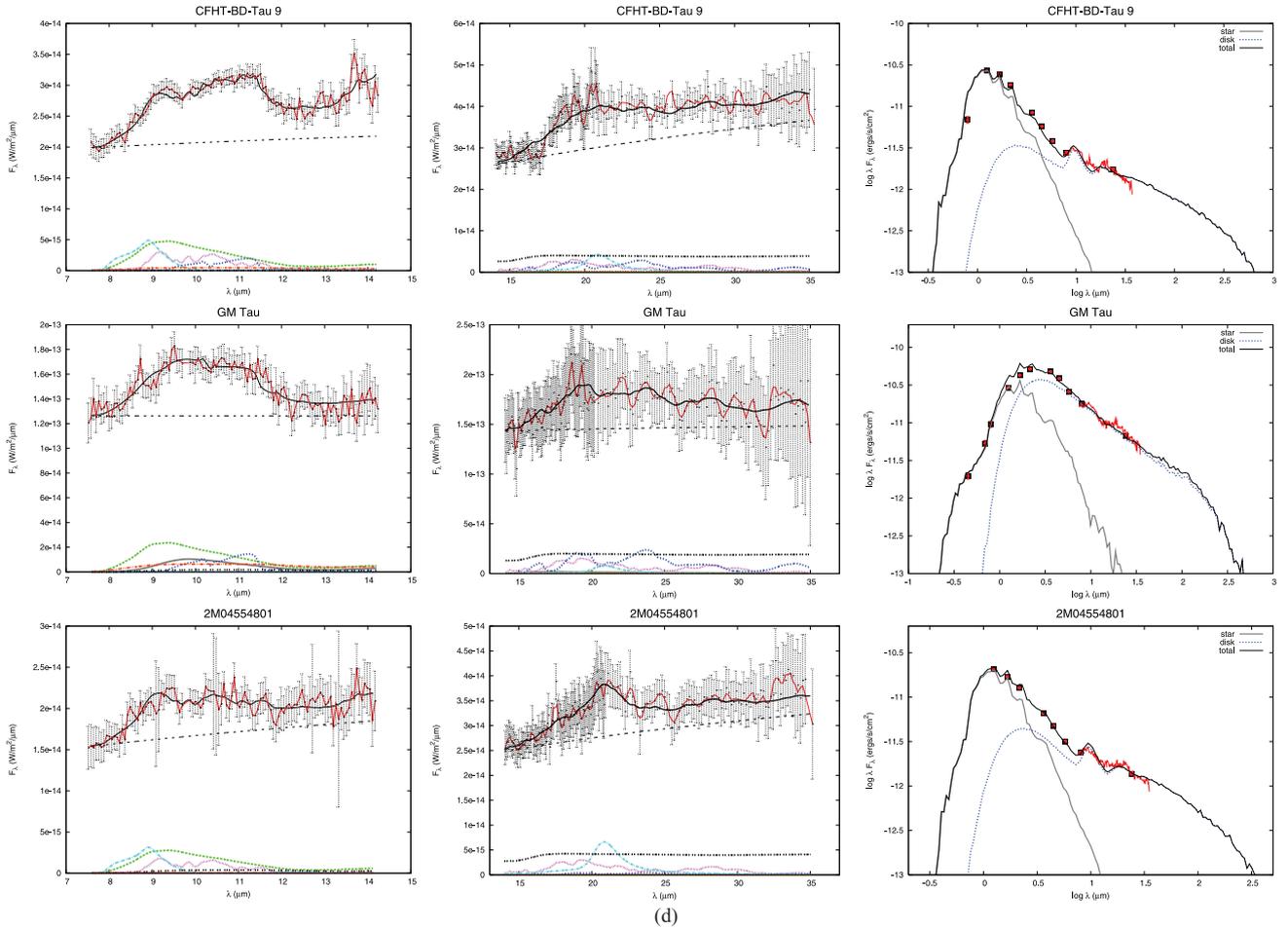
Figure 2 – *continued*

inclination of $i \sim 70°$ (Table 3). An absorption+emission silicate spectrum is sometimes observed for highly inclined discs and can be explained by silicate emission from the disc and silicate absorption from the highly extinguished wall of the disc (e.g. Luhman et al. 2007). While we do not actually see an absorption component for 2M04141188 since the full spectrum lies above the continuum (Fig. 2), the lack of emission indicates larger optical depth in this small disc region, which could be due to the disc's self-absorption at the nearside of the disc. However, if disc self-absorption is evident even at such long wavelengths, one may naturally expect that much more extinction should be observed at much shorter wavelength, which is not seen. It may be that significant dust sedimentation has occurred in this disc region, resulting in the weak emission observed.

4.3 Prominent crystalline forsterite features: 2M04230607, CFHT-BD-Tau 20 and 2M04400067

The 20μm spectrum for 2M04230607 shows prominent crystalline forsterite features at ∼23.8, 27.5 and 34μm. There is another feature observed near ∼16μm which is also indicative of forsterite emission (Fig. 1). In comparison, the 10μm spectrum for 2M04230607 shows a peak near ∼9.3μm, which indicates enstatite emission, while a smaller forsterite peak is observed at ∼11.3μm. The crystalline mass fraction for 2M04230607 shows an increase from ∼38 per cent in the warm inner disc region to ∼57 per cent in the outer cold

region. If we look at the separate contribution from enstatite and forsterite silicates, then the enstatite mass fraction has decreased by a factor of ∼2 in the outer disc, while the forsterite fraction has increased by a factor of ∼3. Such gradients in the dust chemical composition in the inner and outer disc regions have been noted before in discs around solar-type stars and Herbig Ae/Be stars (e.g. van Boekel et al. 2004; Bouwman et al. 2008). 2M04230607 provides a similar interesting case among brown dwarf discs. We discuss the formation mechanism of the different kinds of crystalline silicates in Section 5.4.

The 20μm spectrum for CFHT-BD-Tau 20 also shows a forsterite feature near 34μm. There is a smaller peak observed near 27μm which is also indicative of forsterite emission. The 10μm spectrum is very weak for this object (Fig. 2b), but much stronger emission is observed in the 20μm feature. This suggests the presence of a large mass of cold dust in the disc compared to warm dust in the inner regions. We had discussed in R09 the large uncertainties in the model fits for the 10μm spectrum of CFHT-BD-Tau 20 and the derived mass fractions. The lack of warm dust emission makes it difficult to compare the inner and outer disc mass fractions. From the 20μm model fits, we find a 37 per cent crystalline mass fraction and a 46 per cent fraction of large amorphous grains. It thus exhibits a mixed composition with signs of both grain growth and crystallization in the outer disc. The weak emission from inner surface layers could be due to significant grain growth and dust settling in the inner disc regions. This suggests that dust processing may not
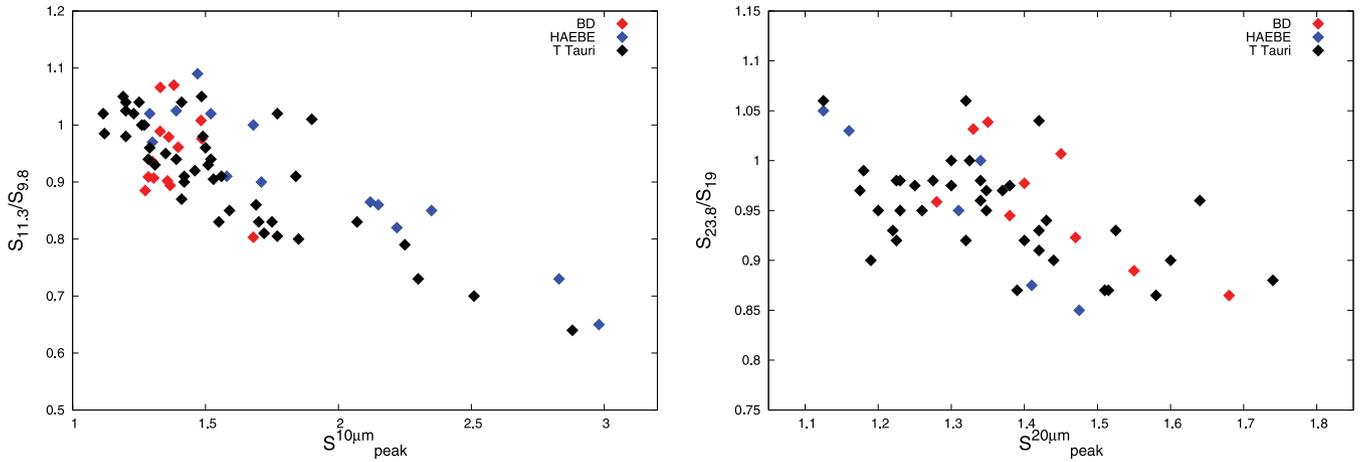
Figure 3. The shape versus strength of the 10 (left) and 20 μm (right) silicate emission features. Colours represent the following: red – Taurus brown dwarfs; blue – Herbig Ae/Be stars; black – T Tauri stars. Data for Herbig Ae/Be stars and T Tauri stars are from van Boekel et al. (2003), Przygodda et al. (2003) and Kessler-Silacci et al. (2005, 2006).

occur on a similar time-scale in the inner and outer regions for all discs. Or there may have been some secondary collisional process that produced this new generation of cold dust in the outer disc regions. CFHT-BD-Tau 20 thus presents an interesting case where the 20 μm emission strength is much higher than that observed in the 10 μm feature, and where large abundances of crystalline silicates are found in the outer cold disc regions.

A similar case is of 2M04400067 that shows broad forsterite features near ∼27 and 34 μm. Some forsterite emission can also be identified near 16 μm. The 10 μm spectrum for this disc shows a broad trapezoidal shaped feature with no prominent crystalline peaks. We find a slight increase in the crystalline fraction from ∼22 per cent in the warm component to ∼30 per cent in the cold region. The inner disc region, however, shows a high fraction of small amorphous grains, with an ∼60 per cent mass fraction, while a high 63 per cent mass fraction is found for the large dust grains in the outer disc region. The outer cold component of this disc thus shows stronger signs of dust processing due to both grain growth and crystallization processes.

The disc model fits for these three discs are shown in Fig. 2(b) (right-hand panel). 2M04230607 shows weak excess emission shortward of ∼8 μm. CFHT-BD-Tau 20 and 2M04400067 show stronger excess emission at these short wavelengths. The scale height at the inner disc edge is slightly higher (by a factor of ∼1.4) for CFHT-BD-Tau 4 than the other two discs. The disc for 2M04400067 shows slight flaring longward of ∼20 μm. For all three discs, the best fits are obtained using an inner disc radius of $1R_{sub}$ (∼0.0004 au) and an intermediate inclination of i ∼50–60°.

4.4 The four 'outlier' cases: MHO 5, CFHT-BD-Tau 8, 2M04290068 and 2M04242090

We have four interesting 'outlier' cases, where the 10 μm feature shows strong silicate emission with a mixed composition of small, large and crystalline grains, but the 20 μm features are very weak, and it is mainly the underlying continuum which is detected (Fig. 2c). This indicates significant dust processing as well as dust settling to the mid-plane in the outer disc regions, while there is still a considerable fraction of warm dust in the inner disc region. For most other discs, we find similar strengths in the 10 and 20 μm features (Section 5.1). We have compared the extent of flaring in

the outer ∼15–35 μm part of the disc for these outliers and the other disc sources, and find similar slopes as observed for the rest. The outlier discs are thus not significantly flatter than the other disc sources that show emission in the 20 μm feature (Fig. 3). It may be that some secondary collisional process has produced this new generation of dust in the inner disc regions, resulting in strong emission at 10 μm, while grains continued to grow and settle in the outer disc. A few of such outliers have also been found among T Tauri stars (e.g. Kessler-Silacci et al. 2007), and have been explained by enhanced dust settling in the outer disc regions. Considering the variety in the disc shapes and structures observed at any given age, such outlier cases suggest that dust processing does not occur on a similar time-scale in the inner and outer regions for all discs.

Results from disc modelling indicate flat disc structures for all four sources. 2M04290068 shows photospheric emission shortward of ∼8 μm and can be classified as a transition disc. From the best-fitting model, we estimate an inner disc hole of ∼$18R_{sub}$ (∼0.006 au), which is a factor of ∼10 larger than the inner disc radius estimated for the other three sources. This system thus seems devoid of disc material in the inner regions of within ∼0.01 au, some emission from the warm surface layers is observed at radii of ∼0.01–0.1 au, while there is an absence of optically thin material at larger radii, as indicated by the flat 20 μm feature.

4.5 CFHT-BD-Tau 9, 2M04554801 and GM Tau

Fig. 2(d) shows model fits for discs with comparatively weak 20 μm features. The S/N for the 20 μm spectra is quite low (∼10). For all three sources, we find very little fraction of small dust grains (<5 per cent) from 20 μm modelling, the crystalline mass fractions are between 20 per cent and 40 per cent and large-grain mass fractions are 50–60 per cent. In comparison with the inner disc fractions, all three sources show an increase in the large-grain and crystalline mass fractions in the outer disc, while the small-grain mass fraction decreases by more than 30 per cent. These discs are thus dominated by more processed dust in the outer regions, which is consistent with the flatter shapes observed for the 20 μm features. The best-fitting model SED is obtained using an inclination of i ∼ 70° for GM Tau, indicating a close to edge-on disc for this brown dwarf. For CFHT-BD-Tau 9 and 2M04554801, a face-on inclination of 30–40° provided the best fit.

The 20µm spectrum for 2M04554801 indicates a silica peak near 20.8µm. In our simplistic model, we have only considered amorphous silica and are able to obtain a good fit to this feature. However, detailed modelling such as that presented in Sargent et al. (2009b) can correctly identify the particular polymorph of silica present in the disc. We find a 27 per cent mass fraction for silica from modelling the 20µm feature, which is the highest silica fraction in the whole sample. Overall, we find silica mass fractions between ∼7 per cent and 14 per cent in the outer regions for these brown dwarf discs, with 0 per cent silica fraction found for V410 X-ray 6 and 2M04141760. As discussed in Sargent et al. (2009b), thermal annealing of olivine and pyroxene produces forsterite and enstatite, along with silica. This silica will be amorphous if annealing takes place at low temperatures (<1000 K) and for short durations. That is, annealing followed by rapid quenching can produce amorphous silica, such as obsidian and tektike. Among T Tauri stars, a few silica exemplars such as ROXs 42C have been modelled by Sargent et al. (2009b), using many different forms of silica including obsidian and amorphous silica. Sargent et al. concluded that annealed silica (a mixture of the two crystalline polymorphs stable at high temperatures and low pressures, cristobalite and tridymite) provides the best fitting of model to spectrum of all the different forms of silica attempted in the models. Annealed silica may also be responsible for the silica feature observed in the 2M04554801 spectrum. Nevertheless, this object presents a similar silica exemplar case among brown dwarfs.

5 DISCUSSION

5.1 Strengths and shapes of the silicate features

Discs dominated by pristine ISM-like dust show flared structures, while flatter structures are observed for the ones that have gone through substantial grain processing. The processing of dust into crystalline silicates and growth to larger sizes both affect the vertical structure of the disc, as well as the emission strength in the silicate features. Fig. 3 compares the strength and shape of the 10 and 20µm silicate features. The shape of the 10µm feature can be estimated by the parameter $S_{11.3}/S_{9.8}$, which is the ratio of the normalized fluxes at 11.3 and 9.8µm (e.g. Bouwman et al. 2001). For the 20µm feature, the shape can be estimated by the flux ratio, $S_{23.8}/S_{19}$. The peaks at 19 and 23.8µm are the most prominent amorphous and crystalline features, respectively, in the ∼15–35µm spectral range (e.g. Kessler-Silacci et al. 2006). Typical uncertainties in the flux ratios are ±0.1. We have included for comparison the data for Herbig Ae/Be stars and T Tauri stars from van Boekel et al. (2003), Przygodda et al. (2003) and Kessler-Silacci et al. (2005, 2006). The strengths of the features are indicated by the S_{peak} values, as discussed above.

An inverse strength–shape correlation can be seen for both the 10 and 20µm features. The correlation is such that spectra with a larger value for the $S_{11.3}/S_{9.8}$ or the $S_{23.8}/S_{19}$ flux ratio have a lower peak-over-continuum flux. This can be explained by the extent of dust processing in the disc; spectra that are dominated by more processed dust due to grain growth and/or crystallization processes are found to be flatter with a peak wavelength close to 11.3µm or 23.8µm, while spectra dominated by unprocessed ISM-like dust show more peaked, narrower profiles with a peak wavelength closer to 9.8 or 19µm. The strength in the feature thus decreases or the feature becomes flatter with increasing crystallinity and/or grain growth in the disc, as indicated by the flux ratios $S_{11.3}/S_{9.8}$ and $S_{23.8}/S_{19}$. This

is more prominent for discs such as V410 X-ray 6 that show weak signs of grain processing and lie in the lower-right part in the plot (S_{peak}^{10} and S_{peak}^{20} ∼ 1.65). 2M04230607, on the other hand, shows strong signs of crystallinity and lies in the upper-left part, near S_{peak}^{10}, S_{peak}^{20} ∼ 1.35, and $S_{11.3}/S_{9.8}$, $S_{23.8}/S_{19}$ ∼ 1.05.

For both silicate spectra, the brown dwarfs show flatter features compared to higher mass T Tauri stars and Herbig Ae/Be stars. We find a clustering for the brown dwarfs near $S_{peak}^{10} \sim S_{peak}^{20} \sim 1.35$. This can be explained by the differences in the location of the silicate emission zone for stars of different luminosities. The silicate feature probes smaller radii (≤1au) in discs around brown dwarfs than in discs around T Tauri stars (≤10au). If crystallization mainly occurs through thermal annealing of amorphous silicates at high temperatures (∼800 K), then this process will be more effective in the inner warm regions. Also, due to the higher densities in the inner disc, we would expect grain growth and dust settling to be more prominent in these regions. Thus due to the smaller radii probed by the silicate features around brown dwarfs, stronger signatures of dust processing would be observed.

Increasing dust processing is thus correlated with weaker strength in the silicate emission feature. In Figs 4 and 5, we have investigated whether the observed flattening and the shift in the peak position of the silicate features are due to an increase in the grain sizes or a higher degree of crystallinity in the disc. The strength in the 10µm silicate feature shows no dependence on the crystalline or the large-grain mass fractions (Fig. 4; left-hand panel). The correlation coefficient is <0.1 for both cases. The 20µm feature strength shows some correlation with the grain growth levels; we find a correlation coefficient of −0.3, at a confidence level of 95 per cent. The correlation is weaker for the 20µm crystalline mass fraction and the 13–35µm spectral slope (correlation coefficient of −0.15 at a 95 per cent confidence level). For the feature shapes (Fig. 5), both the 10µm large-grain and crystalline mass fractions are found to increase as the 11.3µm flux increases relative to the 9.8µm flux. We find a correlation coefficient of 0.4 for both cases at a confidence level of 92 per cent. For the 20µm features, crystallization seems to be more dominant than grain growth in affecting the feature shape (Fig. 5; right-hand panel). The correlation coefficient is 0.34 for the crystallin case (92 per cent confidence level) and 0.02 for the large-grain mass fractions. The feature shape thus seems to be more strongly linked to the crystallization process, while the strength in the features shows some dependence on the grain growth levels in the disc, at least for the 20µm case. The trends we have found for brown dwarfs are consistent with the results seen among higher mass objects in Taurus, as Watson et al. (2009) report both the shape and strength to be strongly linked to the crystallinity in these discs, but no strong correlation is found for the large-grain abundances.

Fig. 6 shows a comparison of the crystalline and large-grain mass fractions with the extent of flaring in the inner and outer disc regions. The extent of flaring in a given disc region can be estimated by the spectral index (α) of the derived continuum from the 10 and 20µm features, using the method defined in Kessler-Silacci et al. (2006). In our definition of α, a more positive value implies higher flaring in the disc. The 10µm crystalline mass fractions show a dependence on the 8–13µm spectral slope. We find a correlation coefficient of −0.4 at a 90 per cent confidence level. In comparison, the correlation coefficient is nearly zero for the large-grain mass fractions. In the outer disc regions, both crystallization and grain growth seem to be effective in causing flattening in the disc. As mentioned, with the exception of V410 X-ray 6, the brown dwarf discs in our sample have flat structures, with similar 15–35µm spectral slopes of ∼−0.5.
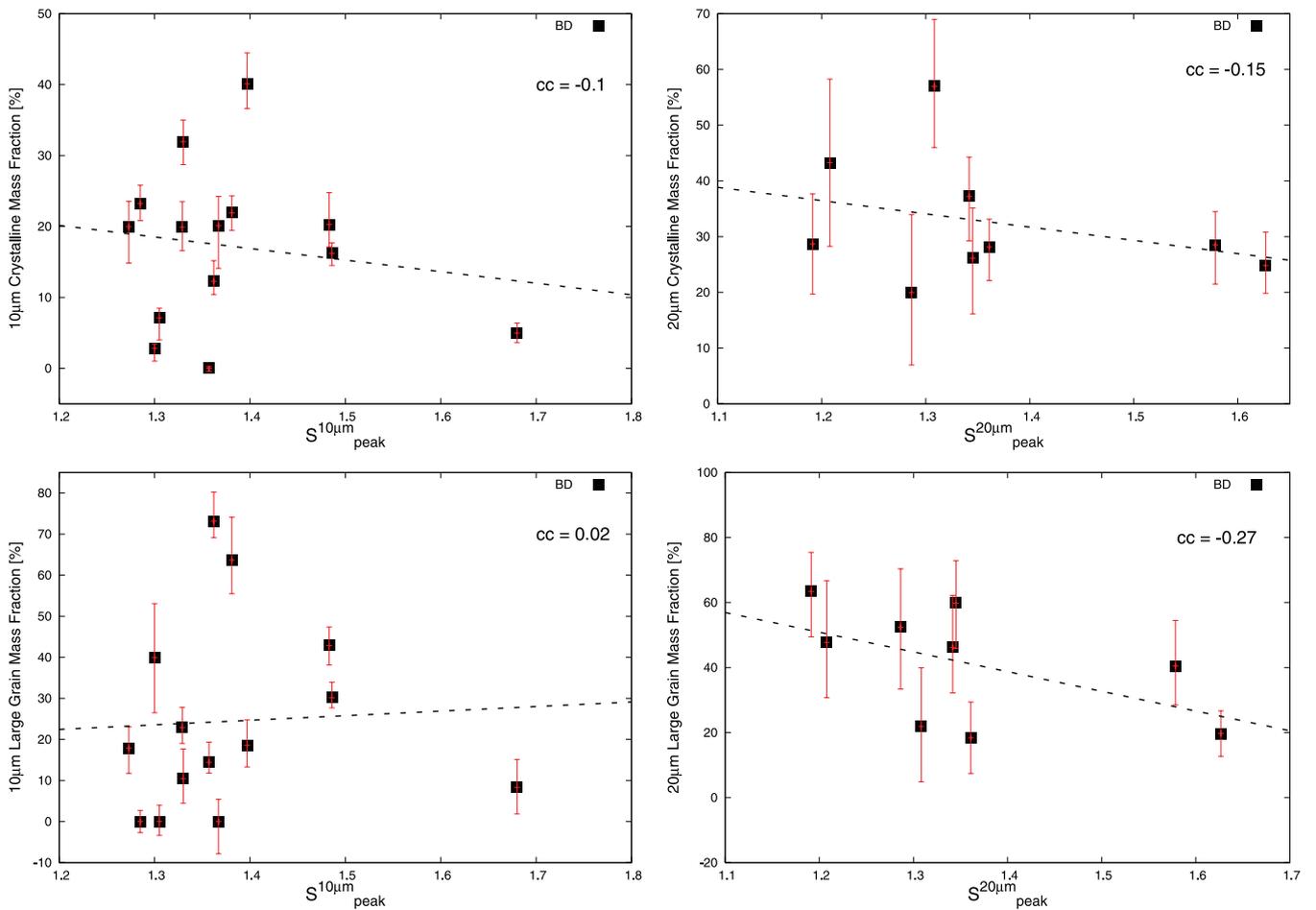
Figure 4. The strength in the 10μm (left) and 20μm (right) features for brown dwarfs versus the crystalline and large-grain mass fractions. The correlation coefficients (cc) are noted in the top-right corner.

Due to the large spread in the mass fractions for similar spectral slopes, the correlation coefficients for the 20μm case are small (∼−0.1). Sargent et al. (2009a) and Watson et al. (2009) have found that the T Tauri discs with the bluest continua at 6-to-13μm and 13-to-31μm wavelengths (the ones with the lowest flaring) tend to have the largest crystalline and large-grain mass fractions. A number of T Tauri stars in the Watson et al. and Sargent et al. samples are found to have flared discs, resulting in a large range in the spectral indices, which makes it easier to identify the possible trends between the disc geometry and the mass fractions. Despite the lack of any strong correlations for the brown dwarfs, we find the strengths/shapes and the extent of flattening in these discs to be affected by both the crystallization and grain growth processes.

The dust settling and sedimentation process resulting in flattening of a disc may also be affected by the level of turbulence in the disc. In discs with higher accretion rates, turbulent mixing may occur alongside grain growth and prolong the time-scales over which large grains settle to the optically thick disc mid-plane (e.g. Dullemond & Dominik 2004). In Fig. 7, there may be some dependence of the grain growth level in the inner disc region on the accretion rate (correlation coefficient = −0.3); MHO 5 and 2M04414825 are among the weakly accreting systems, but show high grain growth levels with ∼70 per cent mass fractions. 2M04141760 is the most actively accreting system in the sample and also has the most least processed disc. CFHT-BD-Tau 6, on the other hand, is also a weakly accreting system but has a large-grain fraction similar to

2M04141760. The accretion rates have been obtained from Muzerolle et al. (2003, 2005). For the case of the 10μm crystalline mass fraction, 2M04141760 is again the only outskirt in the figure, and ignoring this point would result in a flat distribution or a zero correlation coefficient. A flattened disc due to either grain growth and/or crystallization does not necessarily imply a weakly accreting system. However, as noted earlier, nearly all discs in our sample have flattened discs, irrespective of the accretion rate or the mass fractions. In the outer disc region, we find similar levels of grain growth and crystallinity for $\log \dot{M}$ between ∼−8 and −10.5 $M_\odot$ yr^{-1}. The number of known Taurus brown dwarfs with accretion rate measurements is small. A larger number of data points would be valuable to investigate any dependence on the mass accretion rate.

5.2 Inner versus outer disc evolution: dependence on stellar mass

In Fig. 8, we have compared the 10 and 20μm mass fractions for the small and large amorphous grains, and the crystalline silicates. Also included for comparison are data for 65 T Tauri discs in Taurus from Sargent et al. (2009a). The T Tauri sample covers SpT between K5 and M5, which would imply stellar masses between ∼1 and 0.1 $M_\odot$ (using Baraffe et al. 2003 evolutionary models for an age of ∼1 Myr). Our brown dwarf sample consists of a narrow range in SpT between M5 and M7, implying masses of ∼0.1–0.04 $M_\odot$. There is thus no age effect involved in making such a comparison
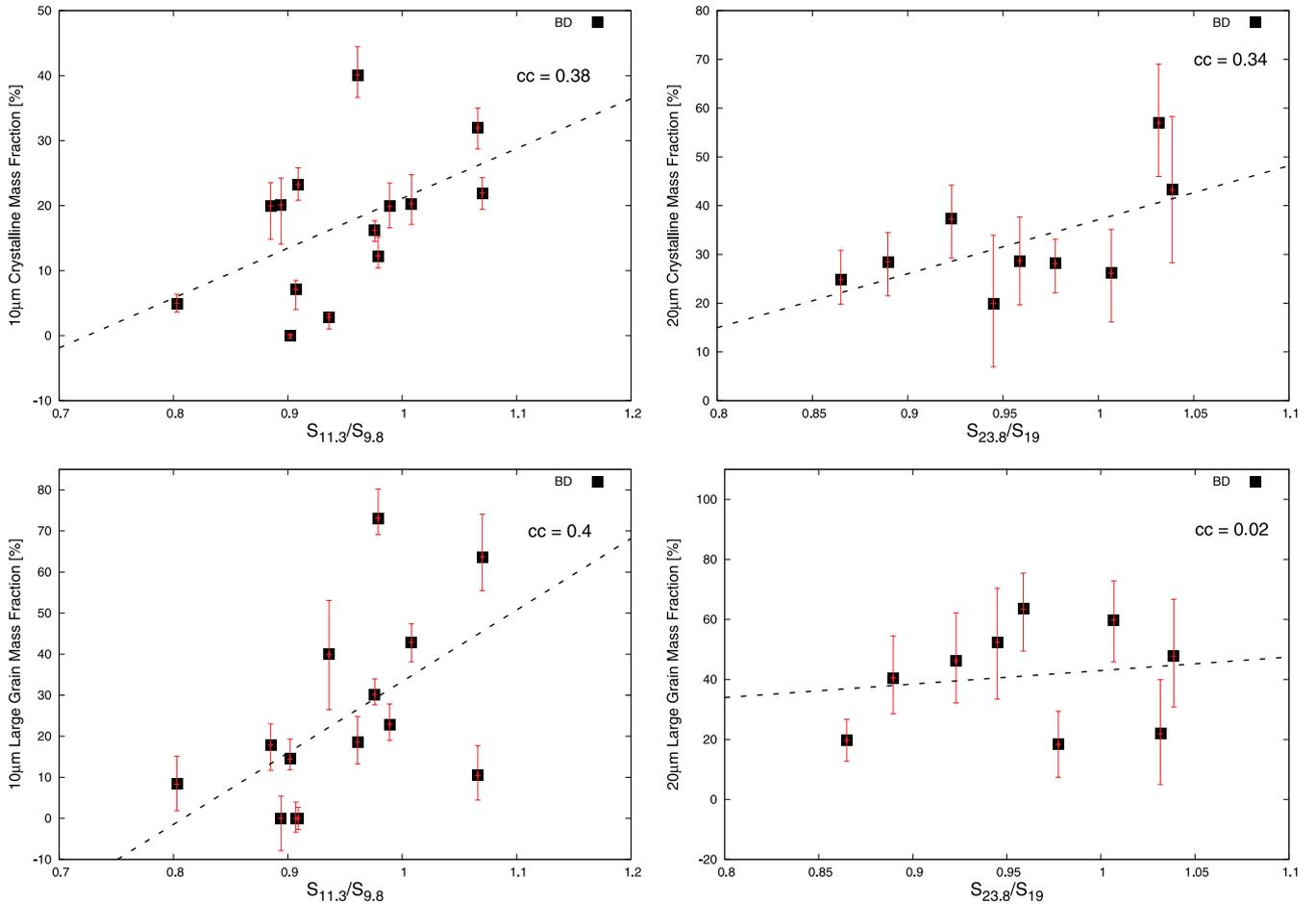
Figure 5. The shape of the 10 μm (left) and 20 μm (right) features for brown dwarfs versus the crystalline and large-grain mass fractions.

as all sources are presumably at the age of Taurus (∼1 Myr). For the Taurus brown dwarfs, more than half of the discs show negligible mass fractions for small amorphous grains in the outer disc regions. We find just two sources that show >50 per cent small-grain mass fractions in both the warm and cold components. These are the two least processed discs discussed in Section 4.1. In comparison, a majority of T Tauri discs have small-amorphous-grain fractions of >50 per cent in the cold component, and in some cases these are much higher than the fractions obtained from the inner disc. When comparing the grain growth levels, most brown dwarfs are shown to have higher large-grain mass fractions in the outer disc. We have six sources that have 10 μm large-grain fractions of <20 per cent, while the outer disc fractions have increased to >20 per cent. Three other brown dwarfs show similar large-grain mass fractions of ∼40 per cent in the warm and cold components. Among the T Tauri samples, nearly all discs show an absence of grain growth in the outer disc region, with a 20 μm large-grain mass fraction of <1 per cent.

If we compare the crystalline levels (Fig. 8; bottom panel), then the T Tauri stars show a large clustering near ∼10 per cent fraction, and almost the full sample has a crystalline mass fraction of ≤20 per cent both in the inner and outer disc regions. The T Tauri distribution also shows two 'tails' of sources with negligible outer disc crystallinity but significant inner disc crystalline mass fractions, and vice versa. Among the brown dwarfs, we find some correlation in the warm and cold crystalline mass fractions, with more than half of the sample showing similar fractions of ∼20–60 per cent at both 10 and 20 μm. The two brown dwarfs with lower crystalline fractions

(<20 per cent) are the two least processed discs of V410 X-ray 6 and 2M04141760. The solid line in Fig. 8(c) is a straight line fit to the brown dwarfs and has a correlation coefficient of 0.5. There is thus (weak) evidence that crystallinity increases linearly from the inner to the outer disc regions for brown dwarfs.

The dependence of the 20 μm mass fractions on the stellar mass can be seen in Fig. 9. There is a lack of later type stars with discs that have abundant small grains, and there is a lack of later type stars with negligible crystalline and large-grain mass fractions. We find a mean 20 μm small, large and crystalline mass fraction of 17.2 per cent, 43.1 per cent and 30.3 per cent, respectively, for the brown dwarfs. In comparison, the higher mass star sample has a mean 20 μm small, large and crystalline mass fraction of 62.2 per cent, 14.7 per cent and 16.1 per cent, respectively. There is thus a factor of ∼2–3 increase in the grain growth and crystallinity levels in the cold disc regions for later type stars, while the fraction of small amorphous grains has decreased by a factor of ∼4.

We thus find two possible trends from our analysis: brown dwarfs show stronger signs of dust processing, in terms of the large-grain and crystalline mass fractions, in the outer disc compared to the inner disc regions, and the extent of dust processing in the cold component is more significant for the substellar discs compared to the T Tauri stars. The trend is more prominent if we consider the four outlier cases discussed in Section 4.4, which show significant grain growth and dust settling in the outer disc regions. Watson et al. (2009) find a trend in the Taurus T Tauri sample of more flattened discs having greater crystallinity. Sargent et al. (2009a) also find a
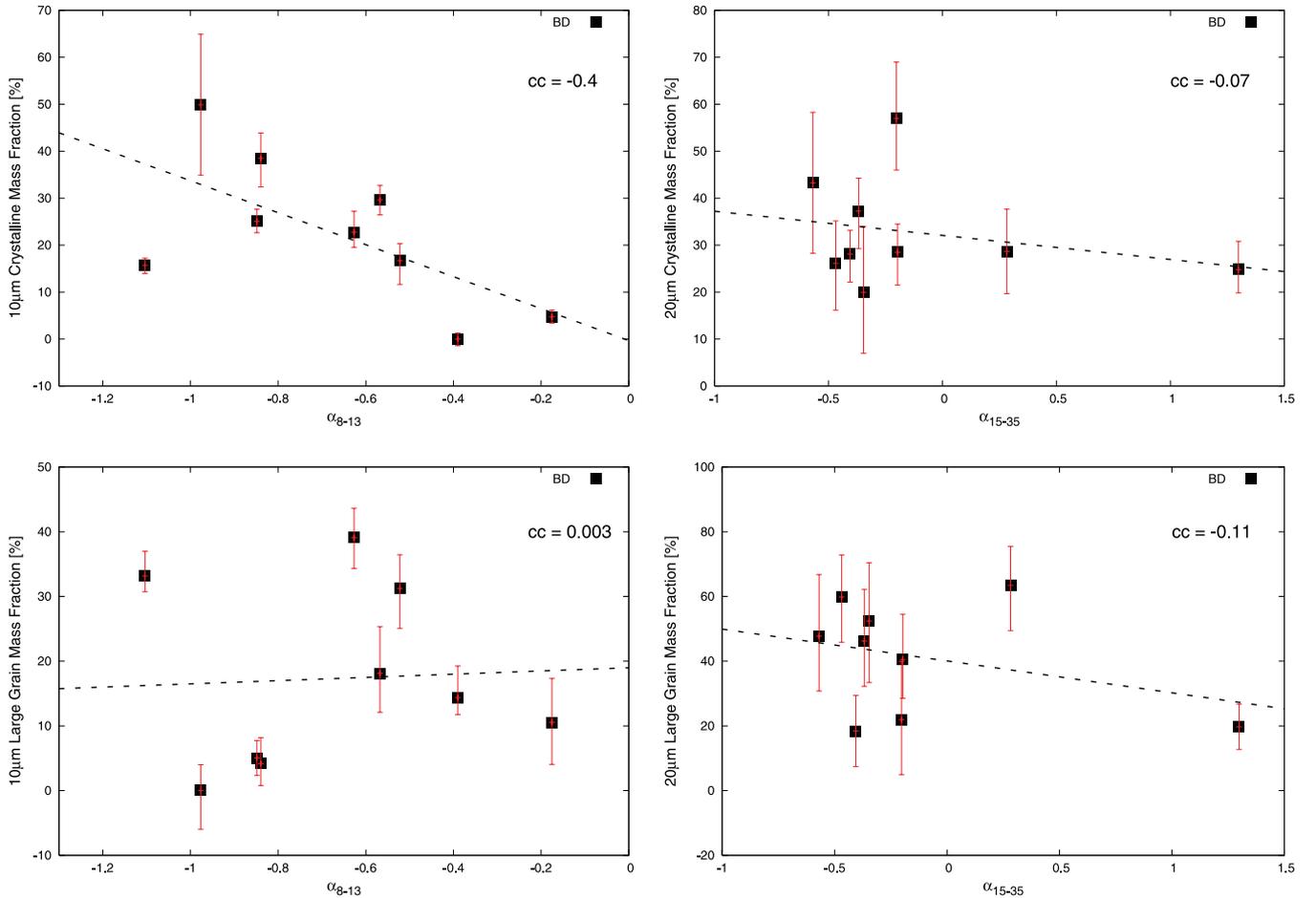
Figure 6. A comparison of the crystalline and large-grain mass fractions for brown dwarfs with the slopes in the inner and outer disc regions, as indicated by the spectral index (α) of the derived continuum from the 10 and 20 µm features.

possible weak trend in a similar sample of flattened discs tending to have higher large-grain mass fractions. For nearly all of our targets, we find a flat disc structure, and so stronger signs of dust processing in terms of higher crystalline and large-grain mass fractions can be expected. V410 X-ray 6 shows a comparatively flared disc structure and has the least processed disc, so the correlation noted by Watson et al. and Sargent et al. also holds true for the substellar cases. Increasing grain growth in the outer disc also suggests that we are looking at a denser region at larger radii for the brown dwarfs, as discussed in Section 5.1. If the 20 µm feature probes lower scale heights or a deeper layer in brown dwarf discs than the surface layers or larger scale heights in T Tauri discs, then we would expect to see grains of larger sizes due to larger density and dust settling for the case of the brown dwarfs. This difference in the disc scale height could also explain the exceptionally high fractions of small dust grains in the cold component of the T Tauri discs (Fig. 9), which are nearly negligible for the case of the brown dwarfs. Small dust grains should be more abundant at larger radii due to decreased densities, but this abundance would decrease with decreasing scale height in the disc, at a given disc radius. We can expect stronger signs of crystallinity in brown dwarf discs compared to T Tauri discs, primarily because the silicate emitting region would lie very close to the central source in brown dwarfs. Using a simple estimation, if the stellar mass drops by an order of magnitude ($1\,M_\odot$ to $> 0.1\,M_\odot$), the disc radius at which annealing temperatures can be reached will be located 10 times closer to the star (e.g. 1 to > 0.1 au)

(Section 3.1). Also, using Kepler's law, $M_* P^2 = A^3$, the Keplerian time will be ~ 10 times smaller if the mass and radius are reduced by a factor of 10. This would lead to very rapid dust evolution around brown dwarfs. Thus due to the whole 10 and 20 µm tracing region lying close to the central source in a brown dwarf disc, stronger signatures of crystallinity would be observed.

5.3 Dependence on X-ray emission strength

Fig. 10(a) compares the crystalline mass fractions with the X-ray luminosity for brown dwarfs and T Tauri stars in Taurus. For the two brown dwarfs 2M04414825 and CFHT-BD-Tau 9, the X-ray luminosities from our new *Chandra* observations are computed in the 0.3–8 keV bands. For the rest of the sources, the luminosities from Grosso et al. (2007) *XMM–Newton* observations are in the 0.5–8 keV range. There is an ~ 10 per cent systematic difference between *Chandra* and the XMM data (~ -0.1 in log L_X). The 10 µm crystalline mass fractions for brown dwarfs show an inverse correlation with the X-ray strength (Fig. 10a; top-left panel). We find a correlation coefficient of -0.6 at a 90 per cent confidence level, obtained from a straight line fit to the plotted points (excluding the upper limits). The dependence is more evident if we compare the 'extreme' cases such as V410 X-ray 6 and 2M04414825, which show weak crystallinity in the disc but are among the stronger X-ray emitters in the sample. No correlation, however, is observed for the 20 µm
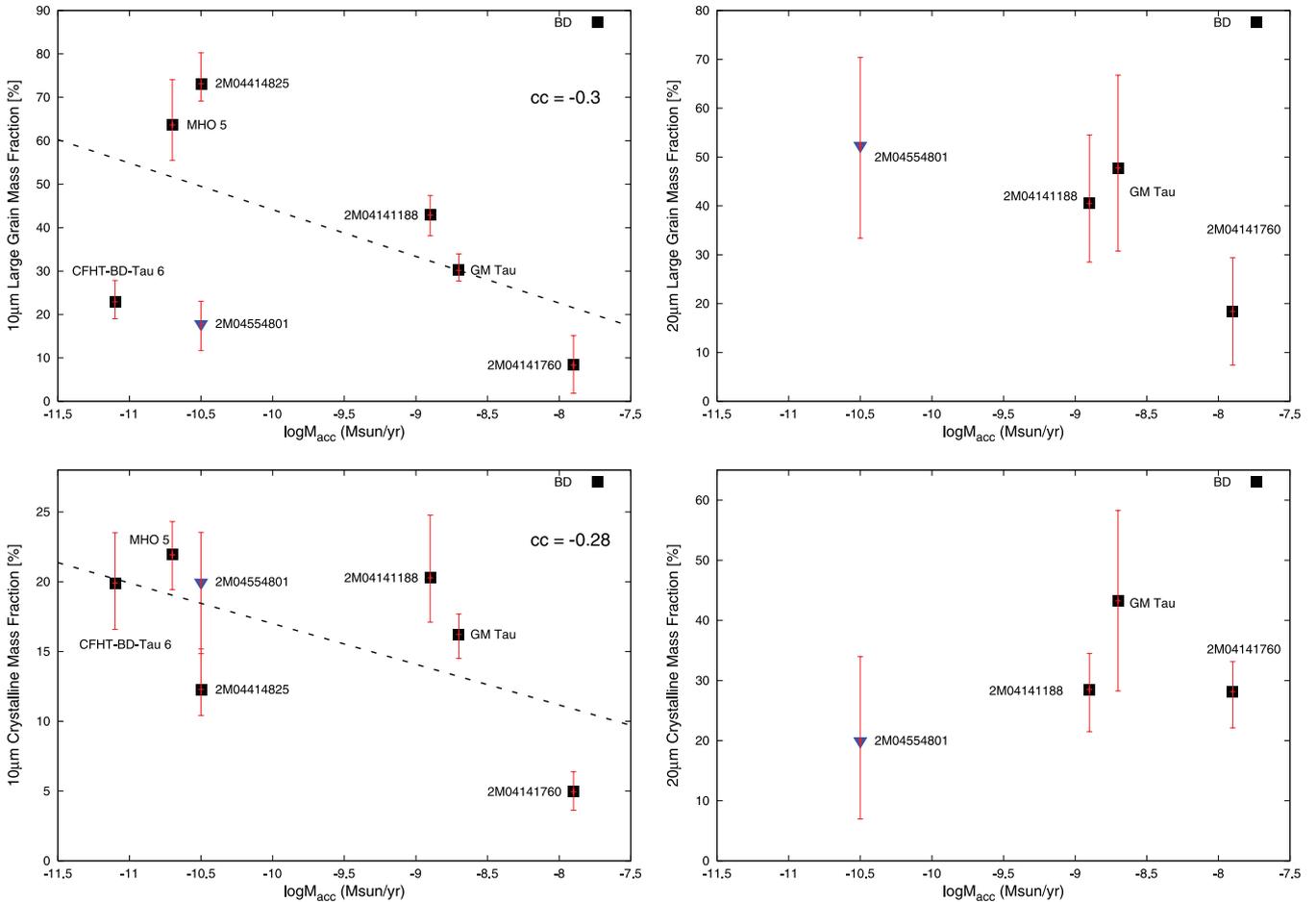
Figure 7. A comparison of the large-grain and crystalline mass fractions for brown dwarfs with the disc mass accretion rates. Upper limits are indicated by blue arrowheads.

crystalline fractions (correlation coefficient = −0.02 at a confidence level of 99.99 per cent), and we find similar mass fractions of ≤20 per cent for a range in X-ray luminosities. Among the T Tauri stars, both the 10 and 20 μm crystalline mass fractions show a nearly flat distribution, and there is no clear dependence observed on the X-ray luminosity. The correlation coefficients are −0.01 to −0.02, at a confidence level of 99.99 per cent. There are, however, five T Tauri sources that show weak X-ray strength ($L_X < 10^{30}$ erg s^{-1}) but high 20 μm crystalline mass fractions of ≥30 per cent (Fig. 10a; bottom-right panel). Though these make up a small ∼7 per cent fraction of the T Tauri sample, there may be a possible inverse trend observed among the weaker X-ray emitters for T Tauri stars.

Fig. 10(b) compares the grain growth levels in the discs with X-ray luminosities. For the case of the brown dwarfs, the 10 μm fractions again show a dependence on the X-ray strength; sources with stronger X-ray emission of $L_X \geq 10^{29}$ erg s^{-1} have higher grain growth levels of >40 per cent. We find a correlation coefficient of 0.42 at a 92 per cent confidence level obtained from a straight line fit to the plotted points. The correlation is again more evident when comparing extreme cases such as 2M04414825 and MHO 5 with V410 Anon 13, which either show very high or negligible fractions of large grains in the disc. A weak anti-correlation may be present for the 20 μm large-grain fractions (correlation coefficient of −0.3 at a 94 per cent confidence level). However, the cold component large-grain fractions have higher uncertainties and we have fewer data points at 20 μm, making it difficult to confirm any

possible trend. Among the T Tauri stars, a large scatter in the 10 μm large-grain mass fractions between 0 and 80 per cent is observed for a range in X-ray luminosities. There are three T Tauri sources with strong X-ray emission ($L_X \geq 10^{30}$ erg s^{-1}) and comparatively higher 20 μm large-grain mass fractions of >40 per cent. But it is unlikely to confirm any X-ray dependence (correlation coefficients <0.05), considering that the cold component large-grain mass fraction is less than 5 per cent for more than 90 per cent of the T Tauri sources.

We have two brown dwarfs in our sample, V410 X-ray 6 and 2M04141760, which have been classified as X-ray flaring sources (Grosso et al. 2007). V410 X-ray 6 is a stronger X-ray emitter and shows variability in L_X between 8×10^{28} and 6.3×10^{29} erg s^{-1}. 2M04141760 shows variability in L_X between 1×10^{28} and 8.5×10^{28} erg s^{-1}. In Fig. 10(a; top-left panel), 2M04141760 is a clear outlier, and the inverse correlation between crystallinity and L_X will be stronger if we ignore this variable source. Similar is the case for the large-grain mass fractions (Fig. 10b; top-left panel), where V410 X-ray 6 is an outlier and ignoring this variable source increases the correlation coefficient between large-grain fractions and L_X to 0.6.

There is thus evidence of a possible anti-correlation between the X-ray emission strength and the crystallinity in the warm component of the discs. Sudden X-ray activity may be responsible for varying the crystalline structure of dust grains in the disc surface layers. If X-ray amorphization happens quickly, then perhaps the maximum X-ray luminosity, as that observed for V410 X-ray 6,
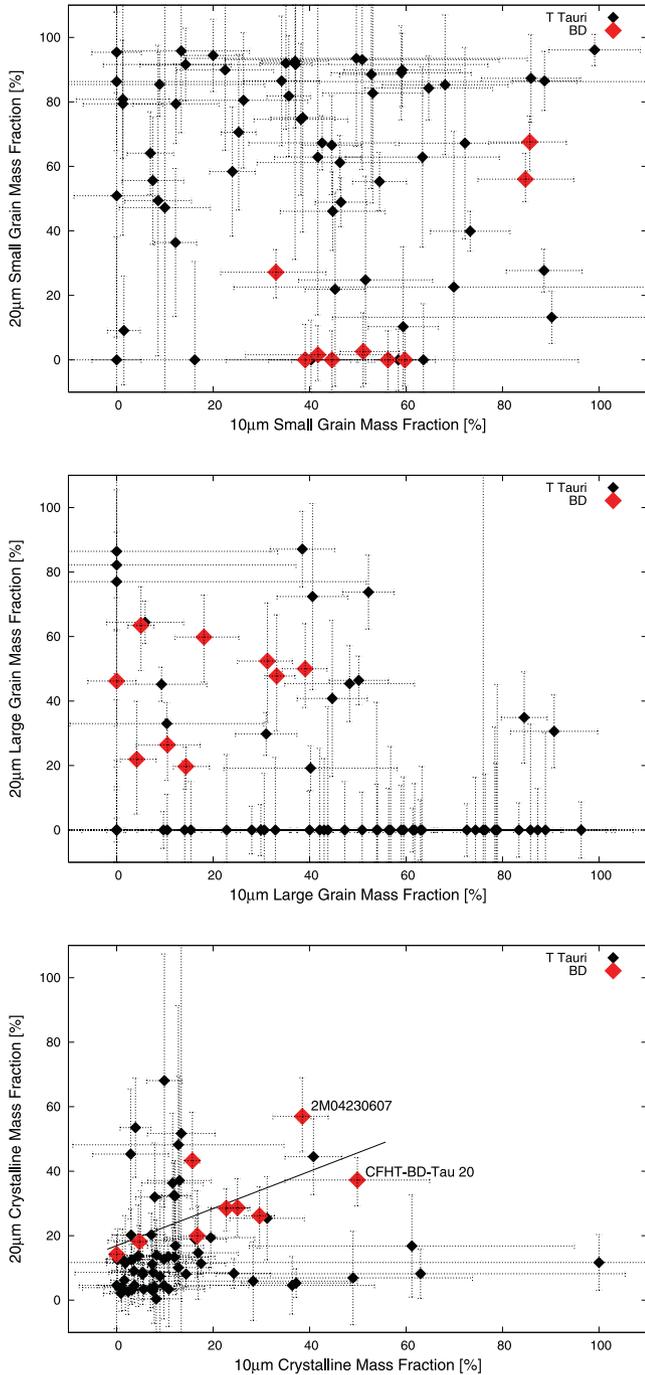
Figure 8. A comparison of the 10 and 20 μm mass fractions for the small amorphous [top panel, (a)], large amorphous [middle panel, (b)] and crystalline grains [bottom panel, (c)]. For the crystalline grains, the solid black line is a straight line fit to the brown dwarf sample. Brown dwarfs are denoted by red symbols, and T Tauri stars by black. The data for T Tauri stars are from Sargent et al. (2009a).

Figure 9. SpT versus the small-grain [top panel, (a)], large-grain [middle panel, (b)] and crystalline [bottom panel, (c)] mass fractions for T Tauri stars and brown dwarfs in Taurus. The value of −2 indicates a SpT of K7, −1 is K5, while 0–7 are M0–M7. Symbols are the same as in Fig. 8.

2M04141760 and 2M04414825, is what directly determines the inner disc crystallinity, rather than some average X-ray luminosity. If we consider only the rightmost points for these objects in the plot in question, then there is a pretty reasonable correlation in the upper-left plots of Figs 10(a) and (b). Processes such as amorphization by ion irradiation have been discussed to explain the absence of crystalline silicates in the ISM (e.g. Jäger et al. 2003; Kemper et al. 2004; Bringa et al. 2007). Some laboratory experiments have
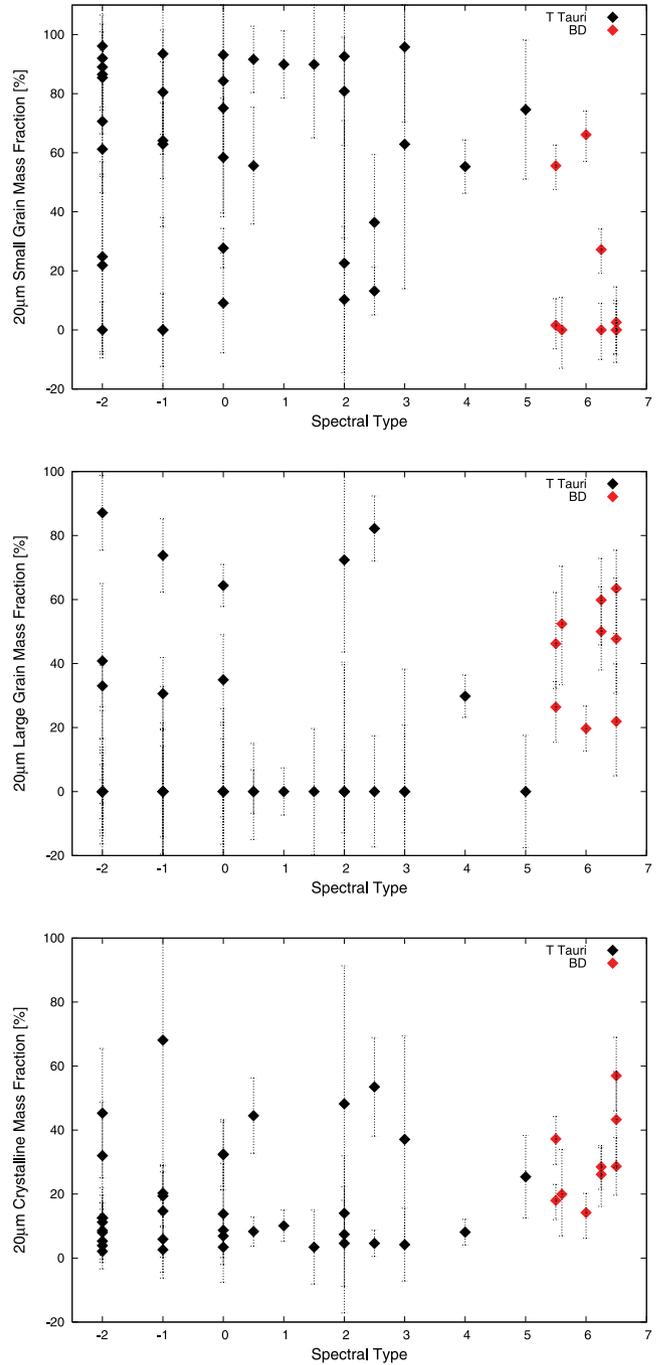
shown low-energy (keV) ions to be efficient in amorphizing silicate dust (e.g. Demyk et al. 2001; Jäger et al. 2003). However, the amophization time-scales estimated by some of these studies are quite long. In the ISM, Kemper et al. (2004) suggest that the amorphization process occurs on a time-scale much shorter than the grain destruction time-scale, and it would take ∼9 Myr to achieve the low crystallinity level observed for the ISM dust (∼0.4 per cent). Bringa et al. (2007) estimate a ∼70 Myr time-scale for amorphization of ISM silicates by heavy-ion cosmic rays at GeV energies. In a study of variability in T Tauri discs, Bary, Leisenring & Skrutskie
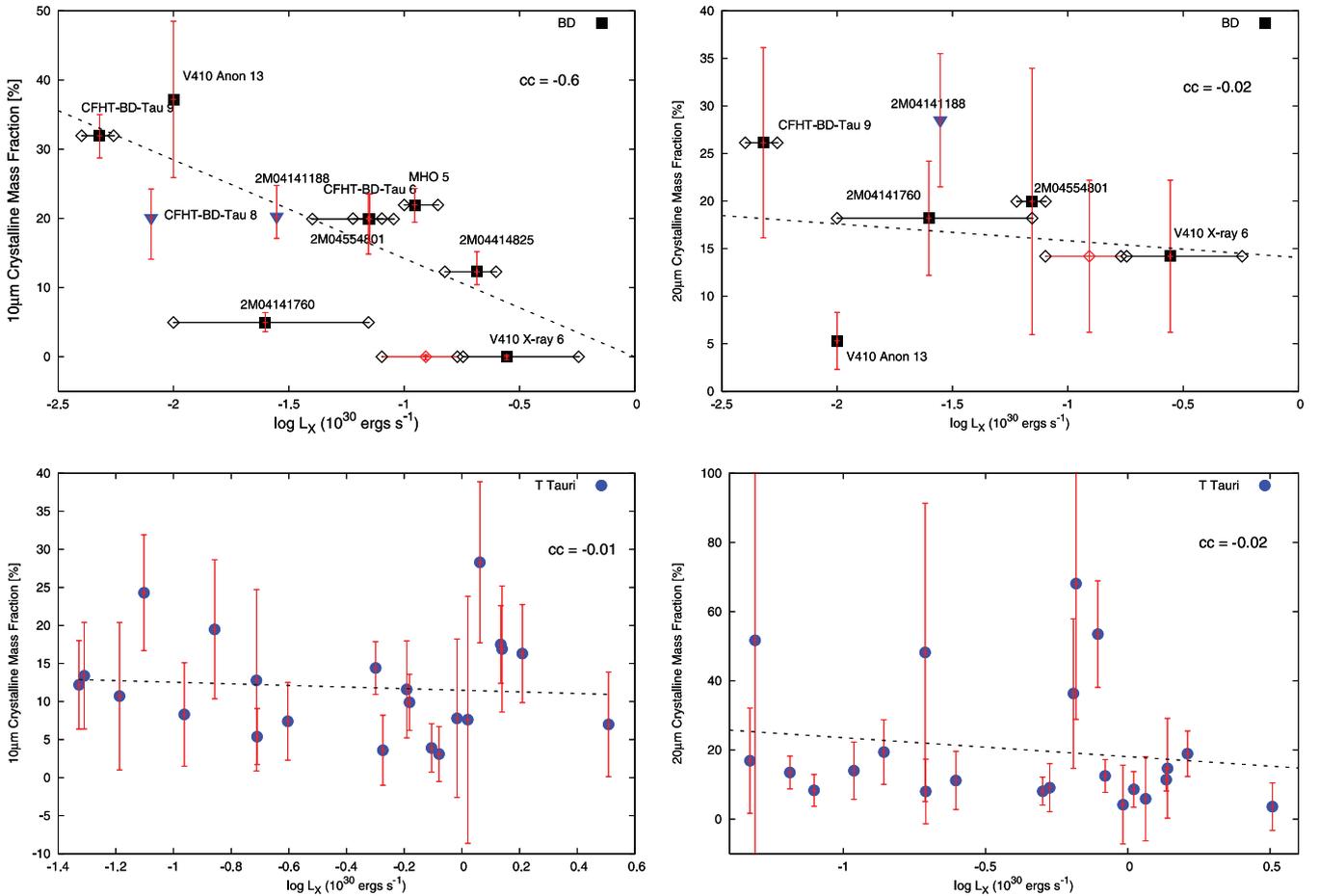
Figure 10. (a) The X-ray luminosity plotted against the crystalline mass fractions (top panel: brown dwarfs; bottom panel: T Tauri stars). The red open diamond denotes the quiescent state for V410 X-ray 6. The black open diamonds mark the range in X-ray emission. Upper limits are indicated by blue arrowheads. (b) The X-ray luminosity plotted against the large-grain mass fractions (top panel: brown dwarfs; bottom panel: T Tauri stars). Symbols are the same as in Fig. 10(a).

(2009) found the 10μm spectra to vary over month- and year-long time-scales, but shorter time-scales on day- to week-long periods were not detected. On the other hand, for the young eruptive star EX Lupi, Ábrahám et al. (2009) obtained a 10μm spectrum just 2 months after an eruption in 2008 and found significant variations when compared with an earlier 2005 silicate spectrum. Ábrahám et al. have noted the fast removal of crystalline silicates to be possibly due to amorphization by X-rays. It is thus difficult to estimate the expected time-scale for the crystalline structure to reform, or otherwise appear in the spectrum. Coronal X-ray emission may correlate with other high energetic radiation in effectively destroying the crystalline silicates, and this may reduce the time-scale over which such processes take place.

An opposite trend is observed for the large dust grains in the warm disc regions for brown dwarfs. Ilgner & Nelson (2006) have considered X-ray irradiation from the central star to be the main source of ionization, and have studied the vertical diffusion of chemical species, that mimics the effects of turbulent mixing in the disc. These authors have shown that X-ray ionization induces turbulence that results in a decrease or a complete removal of the 'dead' zones in the disc. Such zones are defined to be the regions that are too neutral and decoupled from the disc magnetic field for magnetohydrodynamic turbulence to be maintained, as opposed to the 'active' zones that are sufficiently ionized for the gas to be well coupled

to the magnetic field, and thus able to maintain turbulence. M-type pre-main-sequence stars should be fully convective, so they can have strong magnetic fields that could give rise to X-rays. X-rays would therefore be suggestive of a strong stellar magnetic field. The stronger magnetic field then drives a more vigorous Balbus–Hawley instability (Balbus & Hawley 1991) in the disc, which gives rise to turbulence in the disc. Increasing X-ray irradiation could thus be an indirect indicator of the presence of a strong magnetic field, which could result in active turbulent mixing in the disc. With increasing turbulence, the level of sedimentation would decrease and a higher fraction of large grains would be detected in the upper disc layers, as probed by the silicate emission features.

The outer disc crystalline and large-grain mass fractions however are unaffected, which suggests that X-rays cannot penetrate into the surface layers at larger radii in the disc. For the case of T Tauri stars, no clear trend is observed for any of the two processes with the strength in X-ray emission. In Fig. 10, there is a significant overlap in the X-ray luminosities ($-1.4 < \log(L_X) < -0.2$) between the brown dwarf and T Tauri star samples. From the work of Reiners, Basri & Browning (2009), the magnetic field strengths range between 2 and 3 kG for M3–M6 stars. For later types objects at SpT of M7–M9, the field strengths are 1–2 kG (Reiners & Basri 2010). The field strengths for the T Tauri stars and substellar objects are found to be quite similar (~2 kG) at a young age of ~5 Myr
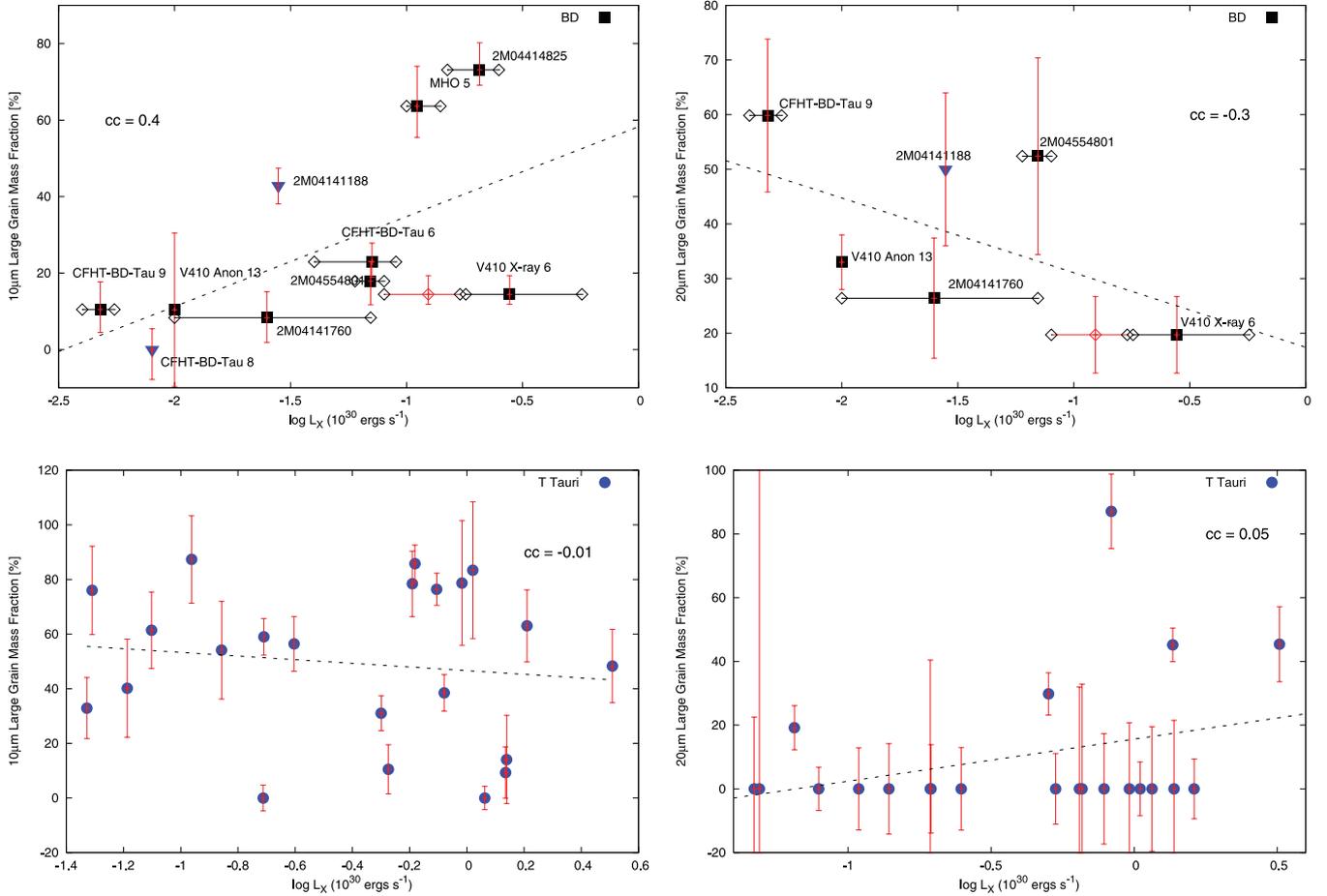
Figure 10 – *continued*

(Reiners & Christensen 2010). The similarity in the magnetic field strengths between T Tauri stars and brown dwarfs implies that any possible correlation found for the brown dwarf mass fractions with X-ray luminosities must also hold true for the T Tauri stars. The lack of any correlation for the T Tauri stars suggests that there may be more decoupled zones in these discs, compared to the substellar cases. Or, perhaps the amorphization process resulting in low crystallinity at high X-ray irradiation (or the opposite process for the grain growth) may occur too quickly or at a much shorter time-scale in T Tauri discs. Such processes may proceed at a slower pace in brown dwarfs, making it possible to study them.

5.4 The presence of crystalline silicates in the cold outer disc regions

A fundamental finding of our work is the almost constant crystallinity observed regardless of the disc radius being probed. Crystalline silicates are certainly not less abundant in the outer cold regions of circum(sub)stellar discs. Two main mechanisms are considered to dominate the crystalline formation: (1) gas-phase condensation at high temperature above ~1200 K; (2) thermal annealing at temperature above ~800 K.

In the gas-phase condensation model, the pristine interstellar dust of olivine and pyroxene composition is transported inwards to the warm inner regions, where these grains are evaporated. The elements of Mg, Si, Fe and O liberated due to evaporation then recondense when the gas cools down to form the forsterite and en-

statite condensates. In the model calculations of Gail (2004), the evaporation rate reaches a peak at a disc radius of ~0.6au, and the pristine dust mixture is completely evaporated within this radius. The inner regions of <0.6au are mainly occupied by the equilibrated components of forsterite and enstatite, although a small fraction of these silicates are also transported in the outer cold regions due to turbulent diffusion and large-scale circulation that mixes the grains inwards and outwards. The abundance of crystalline forsterite and enstatite at 10au is a factor of ~4 less than the abundance at 1au (Gail 2004). This difference in abundances with disc radii could explain, as noted above, the trend of higher crystalline mass fraction for the substellar objects compared to the higher mass stars, as the silicate feature probes smaller radii of ≤1au for brown dwarfs compared to 10–20au for T Tauri discs. Gail (2004) estimates a time-scale of ~1 Myr for the transport, diffusion, annealing, evaporation and recondensation processes and to eventually reach chemical equilibrium, which is consistent with observations.

Fig. 11 compares the enstatite and forsterite mass fractions in the inner and outer disc regions for brown dwarf and T Tauri discs. The 10 and 20µm mass fractions for these dust species in brown dwarfs show a similar range between 0 and ~30 per cent. However, the brown dwarf 2M04230607 is a prominent outlier and shows a higher abundance of forsterite in the outer disc region. Among the T Tauri discs, there are about 10 per cent sources that show a similar high forsterite and enstatite fraction in the cold component of the disc. We consider the case where these different kinds of crystals form through the gas-phase condensation mechanism (e.g.
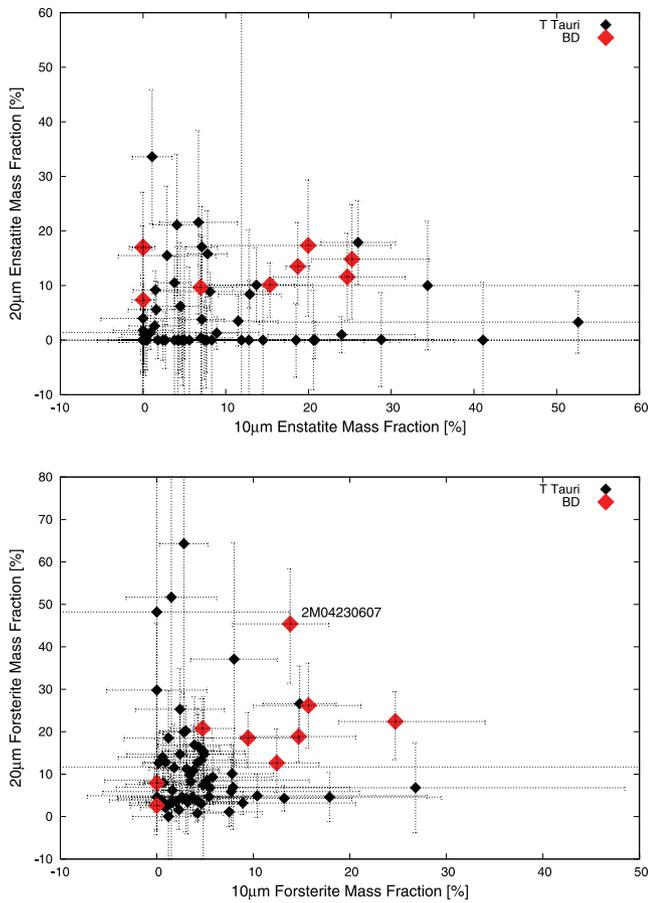
Figure 11. A comparison of the 10 and 20 μm mass fractions for the enstatite (top panel) and forsterite (bottom panel) crystalline silicates. Brown dwarfs are denoted by red symbols, and T Tauri stars by black.

Gail 2004). At high temperatures, forsterite condensates are formed, along with silica (due to dissociation of silicate minerals). This is followed by enstatite formation at a slightly lower temperature due to gas–solid reactions between forsterite and silica. One explanation for the higher forsterite fraction in the outer disc could be that the forsterite at larger radii is not converted to enstatite through solid–gas reactions with silica. This could happen if the surrounding SiO_2 gas is cooled rapidly or if the silica grains coagulate, thus preventing the reactions. We could also consider non-equilibrium conditions in the inner disc, such that only forsterite is formed, and then there is a rapid outward transport of forsterite to prevent reactions with silica to form enstatite. Thereafter, equilibrium conditions may prevail in the inner disc regions (e.g. Bouwman et al. 2008).

Some cases of compositional differences among comets are also known. More specifically, a contrast has been noted between comets with Mg-rich crystals, e.g. Hale–Bopp, which comes from the Oort cloud and probably formed near Jupiter in the giant planet region, and comets with Fe-rich crystals, such as 9P/Tempel 1, which came from the transneptunian region, i.e. further from the Sun (e.g. Keller & Gail 2004; Lisse et al. 2007). This may be indicative of the degree of hydration (or other conditions) in the nebular region where they formed, since Fe-rich silicates hydrate more easily than Mg-rich ones (e.g. Brownlee et al. 2006). Alternatively, the Fe-rich crystals may have formed close to the young Sun (within the present orbit of Mercury), since their annealing requires a high temperature of

~1400 K (e.g. Nuth & Johnson 2006), and then transported outwards to the comet formation zone. The transport, however, must have occurred early on, some 5 to 10 Myr after nebula formation, after which the formation of giant planet cores would have inhibited further radial transport across their orbits (Lisse et al. 2006). Thus, these objects may have formed at different times, as the properties of the dust in the outer nebula evolved from the pre-solar nebula properties (e.g. Lisse et al. 2006; Ciesla 2009). A difference in the location or the times of formation could explain the compositional differences observed for 2M04230607. There may have been a rapid outward transport of crystalline forsterite to prevent reactions with the surrounding silica to form enstatite, resulting in a low enstatite fraction in the outer disc, or forsterite may have formed later in the outer disc due to some in situ formation mechanism, resulting in a high forsterite fraction in the cold component.

There may be some local crystalline formation mechanism occurring in the cold component, such as low-temperature crystallization due to physical or chemical processes that could temporarily raise the local temperature in a turbulent disc environment and cause crystallization, followed by slow cooling over a time-scale of a few seconds (e.g. Molster et al. 1999). A plausible mechanism could be flash heating of dust by shock waves, which has been proposed as a formation mechanism for chondrules found in meteorites (e.g. Harker & Desch 2002). Tanaka et al. (2010) have recently formulated a model in which low-temperature crystallization can be induced by the latent heat of chemical reaction with the ambient gas and may be triggered at temperatures of a few hundred kelvin and at the low gas densities typically observed in the outer regions of a protoplanetary disc. Such non-thermal crystallization could proceed if the heat of reaction is of the order of $10^{26} K cm^{-3}$, and the heat is transferred to the grains on a short time-scale of a millisecond or less. Tanaka et al. have argued that this amount of stored energy density is less than that required for chondrule formation and could be triggered by certain mechanisms likely common in protoplanetary discs such as grain–grain collisions or heating by shock waves due to gravitational instabilities. Interestingly, they find that a higher stored energy density is required to crystallize amorphous silicate of enstatite composition than forsterite composition, suggesting a higher abundance of enstatite in the warm inner region. Their model could provide an alternative to large-scale radial mixing for cases such as 2M04230607, which show a higher fraction of forsterite in the cold component. If both forms of crystalline silicates are formed in the hot inner disc and then transported outwards, similar abundances should be expected throughout the entire disc. A gradient in the dust chemical composition suggests some local crystalline formation mechanism, which could be low-temperature crystallization.

Alternatively, amorphous dust can be thermally annealed into crystalline dust at temperatures above ~1000 K (e.g. Nuth & Johnson 2006), followed by an efficient radial mixing mechanism to transport crystalline material from the hot inner disc to the cold outer parts (e.g. Nuth et al. 2000; Keller & Gail 2004; Okamoto et al. 2004). The very first detection of crystalline silicates in comets, or in any celestial source (except meteorites), was reported by Campins & Ryan (1989). Since then, several comets have been noted to have a high abundance of crystalline dust, e.g. Hale–Bopp has a silicate composition which is ~67 per cent crystalline, while the transneptunian comet Temple 1 has an even higher ~80 per cent crystalline mass fraction (e.g. Lisse et al. 2007). Since these comets are formed in regions much colder than the annealing temperatures in excess of 1000 K, several mechanisms have been proposed to explain the transport of high-temperature silicates from the inner regions of the

solar nebula to the cold outer regions where comets formed. It is interesting to discuss the possible analogies between comets and brown dwarf discs, in terms of the presence of high-temperature material in the cold outer regions, and the mechanisms responsible for their outward transport. Ciesla (2009) has considered the 'jet model' to explain the high abundance of crystalline grains in comet Wild 2 collected by the Stardust spacecraft. Their jet model is similar to the X-wind model from Shu, Shang & Lee (1996). The X-wind model was proposed to launch 'proto-chondrules' as projectiles from the 'X-region' close to the star. These proto-chondrules would be heated to various degrees close to the young Sun and then launched in ballistic trajectories above the disc as a result of winds driven through the interaction of the magnetic field of the Sun with the inner edge of the solar nebula. The proto-chondrules would land back in the outer regions of the disc, which would ordinarily be too cold to melt and crystallize the chondrules.

In the Ciesla (2009) model, jets launched from the inner solar nebula deliver high-temperature materials to the outer comet formation region. The dust grains are injected into the upper disc layers and then vertically diffuse to the disc mid-plane. The abundance of crystalline grains in a comet would be dependent on the delivery time-scale to the outer nebula, or the rate of injection. If the delivery of the high-temperature grains occurs over a short time-scale ($\leq 10^4$ yr), i.e. shorter than the time-scale for radial redistribution, then the crystalline grains can mix with the native amorphous grains, and high crystalline fractions can be achieved in the comets or cometesimals thus formed. If the delivery occurs over a longer time-scale (10^5–10^6 yr), then cometesimal growth would begin in an environment where high-temperature grains are absent, leading to formation of comets with low abundance of high-temperature silicate grains from the inner solar nebula. Such cometesimals could have an outer layer of high-temperature grains that slowly settled to the mid-plane. Thus if the delivery/injection to the outer cold regions occurs over a short time-scale, then a homogeneous mixture would result, while slower delivery would form a heterogeneous comet (Ciesla 2009).

The brown dwarf discs we have studied in this work are at young ages of ∼1 Myr. The high crystalline abundance found in the outer cold regions of 2M04230607 or CFHT-BD-Tau 20 suggests delivery of high-temperature crystalline silicates to the cold regions at an early stage of $<10^4$ yr. Both of these discs also show an ∼20–40 per cent fraction of large amorphous grains, indicating a homogeneous composition which can be expected in the case of early mixing. None of these two sources, however, are known to drive outflows, and so the jet model may not be an applicable mechanism. Nearly a dozen brown dwarf outflow sources have been discovered to date (e.g. Whelan et al. 2009). Two of these outflow sources are found to be rich in crystalline silicates in the inner disc regions (e.g. Phan-Bao et al. 2008; R09), but the outer disc silicate spectrum is either flat or shows amorphous features. Typical outflow mass loss rates for brown dwarfs are between 10^{-10} and 10^{-9} $M_\odot$ yr^{-1} (e.g. Whelan et al. 2009). Perhaps the outflow emission strengths are too weak to efficiently transport high-temperature material to the cold regions. A detailed study of silicate features for the outflow sources will be valuable in determining how effective outflows can be in the radial transport of crystalline silicates.

More than one mechanism may be responsible for the transport of high-temperature silicates. An alternative scenario has recently been presented by Vinković (2009), wherein a non-radial radiation pressure force could loft a crystalline grain several scale heights above the disc mid-plane in the warm inner regions, followed by gliding over the disc surface towards colder disc regions. The grain then re-enters and settles towards lower scale heights when the peak wavelength is larger than the grain size and the radiation force keeping the dust afloat ceases. In the Vinković (2009) model, dust particles of sizes ≤1 mm in optically thick protoplanetary discs are well coupled with the gas. The dynamics of the dust particles are dominated by the gas drag, and dust motion is very similar to the gas orbital, which is almost Keplerian motion. The radiation pressure force serves as the slow perturbation that leads to the rearrangement of dust orbits. The net radiation pressure force is directed exactly parallel to the disc surface irrespective of its curvature. The large grains are thus able to migrate along any disc curvature. Such surface flows might be possible; however, the Vinković model assumes a laminar disc without turbulence. It is not clear if such a gliding process or radiation-pressure mixing is indeed more effective than other process such as turbulent diffusion, X-winds or other mechanisms that could transport crystalline material to the outer region. Nevertheless, the high crystallinity level found in the outer regions for a few of these ∼1 Myr old brown dwarf discs indicates rapid outward transport as well as vertical diffusion during the early stages of formation of these discs.

6 SUMMARY

We present a compositional analysis of the 10 and 20μm silicate emission features for brown dwarf discs in the Taurus–Auriga star-forming region. The spectra show a variety in the emission features characteristic of silicate grains, both amorphous and crystalline in composition. A comparison of the crystalline and large-grain mass fractions in the warm and cold components of the disc, as well as with the higher mass T Tauri stars in Taurus, indicates the following.

(i) Brown dwarfs show stronger signs of dust processing in the cold component compared to T Tauri stars. The grain growth and crystallinity levels in the cold disc regions for later type stars are a factor of ∼2–3 higher compared to the warm component, while the fraction of small amorphous grains is smaller by a factor of ∼4.

(ii) The brown dwarf 2M04230607 provides an interesting case where a difference in the crystalline silicate composition is observed in the inner and outer disc regions; the forsterite mass fraction in the outer disc is a factor of ∼3 higher than the inner disc fraction. Simple large-scale radial mixing cannot account for the gradient in the dust chemical composition and some local crystalline formation mechanism may be effective in this disc.

(iii) We have four 'outlier' cases among the brown dwarfs that show strong 10μm features but very weak 20μm features, implying that significant grain growth/dust settling has occurred at larger radii in these discs. Another outlier case is of CFHT-BD-Tau 20 that shows a weak 10μm feature but strong emission at 20μm. Such outliers suggest that dust processing mechanisms may not proceed simultaneously in the inner and outer regions for all brown dwarf discs.

(iv) *Chandra* X-ray observations have been presented for two Taurus brown dwarfs 2M04414825 and CFHT-BD-Tau 9. These observations were obtained to probe any dependence of crystallization on X-ray emission strength. We find 2M04414825, which has an ∼12 per cent crystalline fraction, to be an order of magnitude brighter in X-ray than CFHT-BD-Tau 9, which has an ∼35 per cent crystalline mass fraction. Combining with previously published X-ray data for brown dwarfs in Taurus, we find the inner disc crystalline mass fraction to be anti-correlated with the X-ray emission strength.

ACKNOWLEDGMENTS

REFERENCES

Ábrahám P. et al., 2009, Nat, 259, 224
Arnaud K., Borkowski K. J., Harrington J. P., 1996, ApJ, 462, 75
Balbus S. A., Hawley J. F., 1991, ApJ, 376, 214
Baraffe I., Chabrier G., Barman T. S., Allard F., Hauschildt P. H., 2003, A&A, 402, 701
Bary J. S., Leisenring J. M., Skrutskie M. F., 2009, ApJ, 706, 168
Bouwman J., Meeus G., de Koter A., Hony S., Dominik C., Waters L. B. F. M., 2001, A&A, 375, 950
Bouwman J. et al., 2008, ApJ, 683, 479
Bouy H. et al., 2008, A&A, 486, 877
Bringa E. M. et al., 2007, ApJ, 662, 372
Broos K. J., Townsley L. K., Getman K. V., Bauer F. E., 2002, ACIS Extract, An ACIS Point Source Extraction Package. Pennsylvania State Univ., University Park, PA
Brownlee D. et al., 2006, Sci, 314, 1711
Campins H., Ryan E. V., 1989, ApJ, 341, 1059
Ciesla F., 2009, Meteoritics Planet. Sci., 44, 1663
Cotera A. S. et al., 2001, ApJ, 556, 958
Damiani F., Maggio A., Micela G., Sciortino S., 1997, ApJ, 483, 370
Demyk K. et al., 2001, A&A, 368, L38
Desch S. J., Connolly H. C., Jr, 2002, Meteoritics Planet. Sci., 37, 183
Dorschner J., Begemann B., Henning T., Jaeger C., Mutschke H., 1995, A&A, 300, 500
Dullemond C. P., Dominik C., 2004, A&A, 421, 1075
Fabian D., Jäger C., Henning Th., Dorschner J., Mutschke H., 2000, A&A, 364, 282
Fabian D., Henning T., Jäger C., Mutschke H., Dorschner J., Wehrhan O., 2001, A&A, 378, 228
Fruscione A. et al., 2006, in Silva D. R., Doxsey R. E., eds, Proc. SPIE Vol. 6270, Observatory Operations: Strategies, Processes, and Systems. SPIE, Bellingham, 62701V
Gail H.-P., 2004, A&A, 413, 571
Grosso N., Audard M., Bouvier J., Briggs K. R., Güdel M., 2007, A&A, 468, 557
Harker D. E., Desch S. J., 2002, ApJ, 565, L109
Hauschildt P. H., Allard F., Baron E., 1999, ApJ, 512, 377
Honda M., Kataza H., Okamoto Y. K., Miyata T., Yamashita T., Sako S., Takubo S., Onaka T., 2003, ApJ, 585, L59
Ilgner M., Nelson R. P., 2006, A&A, 445, 223
Jäger C., Molster F. J., Dorschner J., Henning Th., Mutschke H., Waters L. B. F. M., 1998, A&A, 339, 904
Jäger C., Fabian D., Schrempel F., Dorschner J., Henning Th., Wesch W., 2003, A&A, 401, 57
Juhász A., Henning Th., Bouwman J., Dullemond C. P., Pascucci I., Apai D., 2009, ApJ, 695, 1024
Keller Ch., Gail H.-P., 2004, A&A, 415, 1177
Kemper F., Vriend W. J., Tielens A. G. G. M., 2004, ApJ, 609, 826
Kenyon S., Hartmann L., 1995, ApJS, 101, 117

Kenyon S. J., Dobrzycka D., Hartmann L., 1994, AJ, 108, 1872
Kessler-Silacci J. E., Hillenbrand L. A., Blake G. A., Meyer M. R., 2005, ApJ, 622, 404
Kessler-Silacci J. et al., 2006, ApJ, 639, 275
Kessler-Silacci J. E. et al., 2007, ApJ, 659, 680
Kim S.-H., Martin P. G., Hendry P. D., 1994, ApJ, 422, 164
Li M. P., Zhao G., Li A., 2007, MNRAS, 382, L26
Lisse C. et al., 2006, Sci, 313, 635
Lisse C. M., Kraemer K. E., Nuth J. A., Li A., Joswiak D., 2007, Icarus, 191, 223
Luhman K. L. 2004, ApJ, 617, 1216
Luhman K. L. 2006, ApJ, 645, 676
Luhman K. L., Stauffer J. R., Muench A. A., Rieke G. H., Lada E. A., Bouvier J., Lada C. J., 2003, ApJ, 593, 1093
Luhman K. L., Whitney B. A., Meade M. R., Babler B. L., Indebetouw R., Bracker S., Churchwell E. B., 2006, ApJ, 647, 1180
Luhman K. L. et al., 2007, ApJ, 666, 1219
Luhman K. L., Allen P. R., Espaillat C., Hartmann L., Calvet N., 2010, ApJS, 186, 111
Martín E. L., Delfosse X., Guieu S., 2004, AJ, 127, 449
Merín B. et al., 2007, ApJ, 661, 361
Min M., Hovenier J. W., de Koter A., 2003, A&A, 404, 35
Min M., Hovenier J. W., Waters L. B. F. M., de Koter A., 2008, A&A, 489, 135
Molster F. J. et al., 1999, Nat, 401, 563
Muzerolle J., Hillenbrand L., Calvet N., Briceño C., Hartmann L., 2003, ApJ, 592, 266
Muzerolle J., Luhman K. L., Briceño C., Hartmann L., Calvet N., 2005, ApJ, 625, 906
Nuth J. A., Johnson N. M., 2006, Icarus, 180, 243
Nuth J. A., Hill H. G. M., Kletetschka G., 2000, Nat, 406, 275
Okamoto Y. K. et al., 2004, Nat, 431, 660
Phan-Bao N. et al., 2008, ApJ, 689, L141
Preibisch T., Zinnecker H., 1999, AJ, 117, 2381
Przygodda, van Boekel R., Àbrahàm P., Melnikov S. Y., Waters L. B. F. M., Leinert Ch., 2003, A&A, 412, L43
Reiners A., Basri G., 2010, ApJ, 710, 924
Reiners A., Basri G., Browning M., 2009, ApJ, 692, 538
Reiners A., Christensen U. R., 2010, A&A, 522, A13
Riaz B., 2009, ApJ, 701, 571 (R09)
Riaz B., Gizis J. E., 2007, ApJ, 661, 354
Sargent B. et al., 2009a, ApJS, 182, 477
Sargent B. et al., 2009b, ApJ, 690, 1193
Scholz A., Jayawardhana R., Wood K., 2006, ApJ, 645, 1498
Shu F. H., Shang H., Lee T., 1996, Sci, 271, 1545
Tanaka K. K., Yamamoto T., Kimura H., 2010, ApJ, 717, 586
van Boekel R., Waters L. B. F. M., Dominik C., Bouwman J., de Koter A., Dullemond C. P., Paresce F., 2003, A&A, 400, L21
van Boekel R. et al., 2004, Nat, 432, 479
van Boekel R., Min M., Waters L. B. F. M., de Koter A., Dominik C., van den Ancker M. E., Bouwman J., 2005, A&A, 437, 189
Vinković D., 2009, Nat, 459, 227
Walker C., Wood K., Lada C. J., Robitaille T., Bjorkman J. E., Whitney B., 2004, MNRAS, 351, 607
Watson D. et al., 2009, ApJS, 180, 84
Whelan E. T., Ray T. P., Podio L., Bacciotti F., Randich S., 2009, ApJ, 706, 1054
Whitney B. A., Wood K., Bjorkman J. E., Cohen M., 2003, ApJ, 598, 1079
Wood K., Wolff M. J., Bjorkman J. E., Whitney B., 2002, ApJ, 564, 887
Wooden D. H., 2008, Space Sci. Rev., 138, 75
Zolensky M. E. et al., 2006, Sci, 314, 1735

This paper has been typeset from a TeX/LaTeX file prepared by the author.